Received: 23 July 2020 | Revised: 17 December 2020 | Accepted: 22 December 2020

DOI: 10.1002/dep2.135

ORIGINAL RESEARCH ARTICLE

The Depositional Record Open Access
A journal of the International Association of Sedimentologists
IAS
WILEY

Unravelling the pore network and its behaviour: An integrated NMR, MICP, XCT and petrographical study of continental spring carbonates from the Ballık area, SW Turkey

Jeroen Soete[1,2] | **Steven Claes**[2,3] | **Hannes Claes**[2,4] | **Marcelle M. Erthal**[2,5] | **Helen Hamaekers**[2,6] | **Eva De Boever**[7] | **Anneleen Foubert**[6] | **Norbert Klitzsch**[8] | **Rudy Swennen**[2]

[1]Materials Engineering, KU Leuven, Heverlee, Belgium

[2]Earth and Environmental Sciences, KU Leuven, Heverlee, Belgium

[3]Flemish Institute for Technological Research (VITO), Mol, Belgium

[4]Clay and Interface Mineralogy (CIM), RWTH Aachen, Aachen, Germany

[5]Petrobras Research Center, Ilha do Fundão, RJ, Brazil

[6]Geosciences, Université de Fribourg, Fribourg, Switzerland

[7]Geological Survey of the Netherlands – Part of TNO, Utrecht, The Netherlands

[8]Applied Geophysics, E.ON ERC, RWTH Aachen, Aachen, Germany

Correspondence
Jeroen Soete, Materials Engineering, KU Leuven, Kasteelpark Arenberg 44, 3001, Heverlee, Belgium.
Email: jeroen.soete@kuleuven.be

Abstract

Applying an integrated methodology, including petrography, mercury injection capillary pressure, laboratory nuclear magnetic resonance and X-ray computed tomography, on continental spring carbonate reservoir analogue samples is a prerequisite to understand plug scale porosity and permeability heterogeneities. Depending on the dominant pore type in a sample, the orientation and distribution of the pores, pore network connectivity varies from poor to excellent in these continental spring carbonates. The latter exhibit large-scale ranges for both porosity (3%–25%) and permeability (0.004–3,675 mD). Facies classification alone proved insufficient to link porosity and permeability, due to intrafacies pore network variability. Better assessment of reservoir properties can be achieved by subdividing facies into lithotype and pore type classes. Obtained pore network data addresses the pore types, pore (throat) sizes, number of pore compartments, and allow a subdivision of the pore size distributions into unimodal, bimodal and atypical types. There is no micropore compartment present in samples with unimodal mercury injection capillary pressure and nuclear magnetic resonance distributions. Decoupled micropore compartments are observed in samples with bimodal mercury injection capillary pressure and nuclear magnetic resonance distributions, which show isolating calcite rims, and have limited permeabilities. The cement rims decrease the macropore connectivity and decouple the micropore compartments, which reside in micritic dendrites. The micropore compartment ($r < 1$ μm) is coupled with the mesopore ($r = 1$–15 μm) and macropore compartment ($r > 15$ μm) for atypical samples which lack pore-lining calcite rims.

KEYWORDS

continental spring carbonates, MICP, NMR, permeability, pore types, porosity, XCT

1 | INTRODUCTION

The unceasing usage of hydrocarbons as an energy resource made developing the most complex carbonate reservoirs economically profitable. Worldwide, porous carbonate rocks, including 'supergiant fields' in the Middle East (Nurmi & Standen, 1997) produce around 40% of all oil and gas. Recent discoveries of continental carbonate reservoirs have highlighted the reservoir potential of these rock types in the so-called Presalt exploration, offshore Brazil (Terra et al., 2010; Wright, 2012) and in the Namibe Basin, Angola (Saller et al., 2016; Schröder et al., 2016; Sharp et al., 2013). The Presalt carbonates are mainly deposited in lacustrine environments, where carbonates that are diagnostic of hydrothermal springs, i.e. travertines, were also observed (Schröder et al., 2016). Microbial and abiotic continental spring carbonate precipitates have excellent hydrocarbon potential (Rezende & Pope, 2015). The precipitates act as a strong framework that resists compaction and has the potential to preserve primary porosity (Eberli et al., 2003; Soete et al., 2015). Further understanding of spring carbonates is crucial in the exploration and development of carbonate reservoirs in rift basins (Mancini et al., 2013). Their sedimentology has been widely studied (Della Porta et al., 2017; Erthal et al., 2017; Ford & Pedley, 1996; Guo & Riding, 1998; Pedley & Rogerson, 2010; Pentecost, 2005; Wright & Barnett, 2015). Khatib et al. (2014) and Lebatard et al. (2014) even performed a porosity study as a side project of their palaeomagnetic dating, but it was not until recently that considerable research was devoted to, and focussed on rock petrophysics, i.e., porosity, permeability and acoustic velocities (Claes et al., 2017a, 2017b; De Boever et al., 2017; Ronchi & Cruciani, 2015; Saldaña et al., 2020; Soete et al., 2015, 2017; Török et al., 2017). Carbonate lithologies contain some of the most complex pore networks, shaped by various processes active during carbonate precipitation and modified during diagenesis (Brigaud et al., 2014; Claes et al., 2015; Dewit et al., 2012; Erdoğan & Özvan, 2015; Lapponi et al., 2011; Nurmi & Standen, 1997; Soete et al., 2015). Classifying pore types and measuring pore sizes are well established practices in reservoir geology (Claes et al., 2016), however, the contribution of these different pore types to the pore network connectivity is often poorly understood and greatly reduces flow predictability. Therefore, recognising pore compartments, i.e., assemblages of interconnected and communicating pore types, within the pore network of carbonates is necessary to develop improved conceptual reservoir models (Brigaud et al., 2014; Eberli et al., 2003; Ehrenberg et al., 2006; Lucia, 2007; Nurmi & Standen, 1997). Integrating petrophysical methods over multiple scales is necessary in order to maximise the capture of heterogeneities (Alabi et al., 2014). Nuclear magnetic resonance (NMR) logging is one of the preferred methods for porosity measurement in reservoirs due to the techniques relative insensitivity to changes in mineralogy and its reliability in estimating permeability (Boyd et al., 2015). Nuclear magnetic resonance, after calibration with laboratory measurements, consequently plays a central role in addressing complex pore geometries and other heterogeneities, certainly in combination with X-ray computed tomography (XCT; Alabi et al., 2014; Belila et al., 2020; Chitale et al., 2014; Diniz-Ferreira & Torres-Verdín, 2012). In this paper, an integrated methodology for characterising the pore network, including petrography, XCT, mercury injection capillary pressure (MICP) and laboratory NMR is tested. Such an integrated approach allows pore sizes from nano to centimetre scale to be studied. Nuclear magnetic resonance is a technique that, when combined with more traditional techniques, such as petrography and MICP, has the ability to provide crucial information regarding pore size distributions (PSD), porosity and indirectly the connectivity between pore compartments and permeability (Fleury et al., 2001; Minh et al., 1997; Nurmi & Standen, 1997; Vincent et al., 2011; Westphal et al., 2005). The pore throat sizes, measured with MICP, are an important additional parameter, because permeability is controlled by throat sizes, rather than by the pore body volume (Rezaee et al., 2006). This study applies an integrated approach to identify pore compartments in continental spring carbonates in a reservoir analogue and characterises their role, with regard to flow through the pore network, as a function of the different lithotypes, pore types and sizes present within these compartments.

2 | GEOLOGICAL SETTING

This study examines continental spring carbonate samples from the Faber and Ece quarries, situated in the Ballık area, near Denizli in Turkey (Figure 1A), at the northern edge of the Denizli Basin (Figure 1B; Özkul et al., 2013). The plate tectonic history of western Turkey, including uplift in a plate collision setting and subsequent orogenic collapse, resulted in the formation of horst and graben structures (van Hinsbergen et al., 2010; Van Noten et al., 2013, 2019). The Quaternary Denizli Basin represents such horst and graben morphologies and is composed of two sub-basins, the Çürüksu and Laodikeia grabens. The Çürüksu Graben, of interest in this study, is a Neogene-Quaternary depression. The graben is the continuation of the EW-trending Büyük Menderes Graben and the NW–SE-trending Gediz Graben. The Quaternary deposits consist of the Tosunlar Formation, which are locally covered by alluvium, alluvial fan and Pleistocene continental spring carbonate deposits (Alçiçek, et al., 2007; Bozkurt & Bozkurt, 2009; Gürer & Yilmaz, 2002; Kele et al., 2011; Lopez et al., 2017). Earlier studies of the Ballık continental spring carbonates included the mapping of faults, fractures and fissures. The mapping allowed continental spring carbonate formation to be linked with seismically active areas

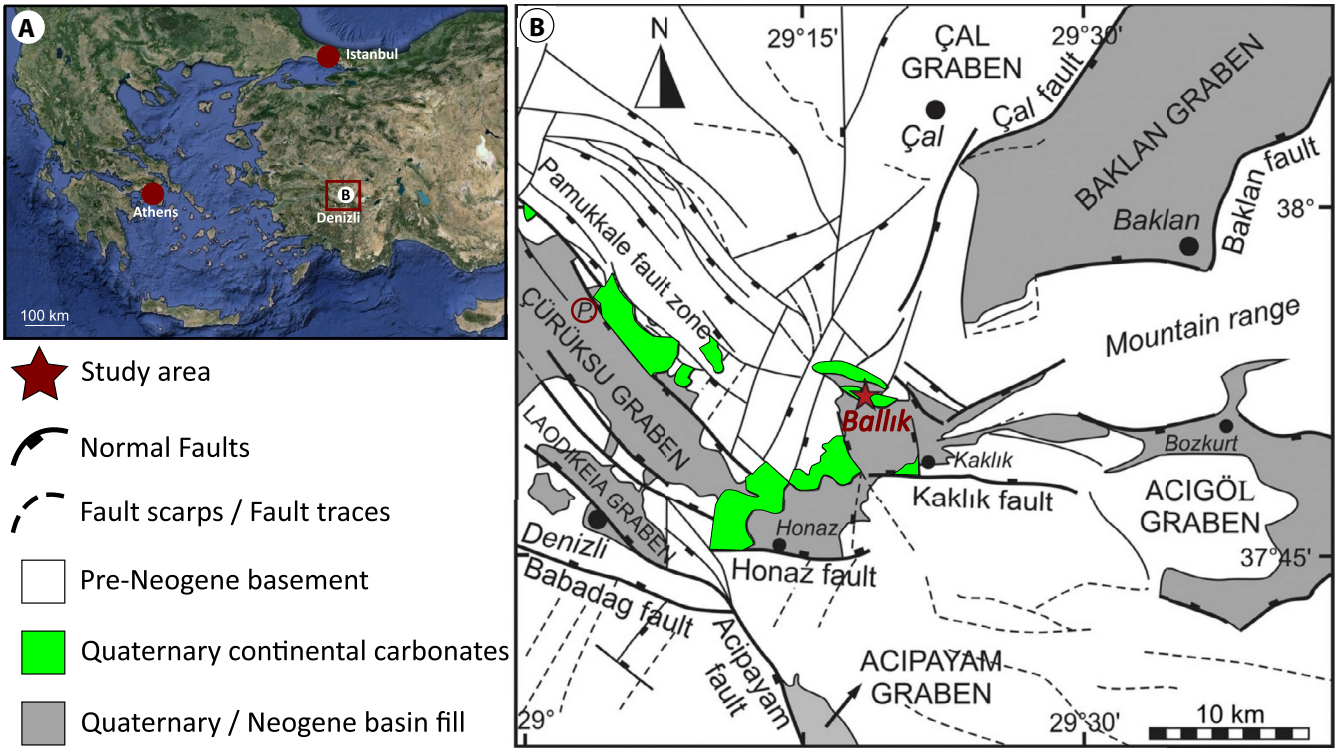

FIGURE 1 (A) Regional map and (B) geological map of the Denizli Basin, Pamukkale (P.) and its surroundings, with indication of the Ballık area (red star). Map adapted from Landsat ETM images and SRTM data after Gürbüz et al. (2012), Kaymakci (2006), Koçyiğit and Deveci (2007) in Van Noten et al. (2013)

and to the tectonic context of the Denizli Basin (De Filippis et al., 2012; Hancock et al., 2000; Van Noten et al., 2013, 2019). The continental spring carbonates, including the world heritage site of Pamukkale (UNESCO World Heritage Centre, 1992–2015), occur along the basin-bounding NW-SE, E-W and NNE-SSW oriented fault zones of the Denizli Basin (Figure 1B).

The Ece and Faber quarries are part of a Pleistocene (>550 ka; Claes et al., 2020) domal continental spring carbonate structure (Van Noten et al., 2013), which is one of many continental spring carbonate bodies that formed in between the alluvial strata. This study profits from extensive background data on the studied site from other work, including detailed sedimentological and geochemical characterisations (Aratman et al., 2020; Claes et al., 2015, 2017b, 2019; De Boever et al., 2017; Mohammadi et al., 2020; Özkul *et al*., 2002). El Desouky et al. (2015) used microthermometry on fluid inclusions of cement phases and strontium isotopes to constrain the source rock for the supply of calcium (Ca^{2+}) and bicarbonate (HCO_3^-) ions. According to the latter authors, meteoric recharge water that infiltrated the subsurface in the nearby mountain regions likely came in contact with, and started to dissolve the Lycian nappe Mesozoic carbonates and evaporites. Active tectonics, with associated normal faulting, provided pathways for the infiltrated fluids to resurface along numerous springs. The Ballık continental spring carbonates (Figure 1) are situated near the junction of the NW-SE-trending Çürüksu Graben, the adjacent NE-SW-trending Baklan Graben and the EW-oriented Acıgöl Graben (Van Noten et al., 2013). Nearby active continental spring carbonate precipitation demonstrates that both ambient temperature springs and hot springs were present in the environment (Claes et al., 2015). For example the Kaklik cave, situated about 5 km from the study area, has a present day ambient temperature spring of around 22.8°C, while the Çukurbağ thermal spring on the Pamukkale site has a present day temperature of 57.1°C (Özkul et al., 2013).

3 | METHODOLOGY

The methods and instruments that were applied for the characterisation of the continental spring carbonate pore network are discussed below.

3.1 | Optical microscopy and scanning electron microscopy

The optical petrography was conducted with polarized light microscopy (PLM) and fluorescence microscopy (FM). Samples were impregnated twice under vacuum conditions with dyed epoxy before thin section preparation. The fluorescent dye allowed the (micro)porosity to be studied with

transmitted, but especially with incident fluorescent light microscopy. Scanning electron microscopy (SEM) was used for the visualisation of small-scale textures and pores. The photomicrographs of samples coated with gold were taken with a JEOL JSM-6400 SEM. The accelerating voltage used in this study was 10–15 kV, with an emission current of approximately 300 μA.

3.2 | Core analysis

The petrophysical measurements were conducted on 42 plugs with a diameter of 1 inch (2.54 cm). Water saturation experiments were carried out first. The dry weight, saturated weight and submerged weight of the samples allowed the bulk volume (Equation 1), grain volume (Equation 2), bulk density (Equation 3), grain density (Equation 4) and porosity (Equation 5) to be calculated for each sample (Crain, 2019).

$$V_b = \left(m_{sat} - m_{sub}\right) / \rho_{fl} \tag{1}$$

$$V_g = \left(m_{dry} - m_{sub}\right) / \rho_{fl} \tag{2}$$

$$\rho_{bulk} = m_{sat} / V_b \tag{3}$$

$$\rho_{grain} = m_{dry} / V_g \tag{4}$$

Finally Archimedes porosity is described as:

$$100 \left[\left(m_{sat} - m_{dry}\right) / \left(m_{sat} - m_{sub}\right)\right] \tag{5}$$

with V_b is the bulk volume, V_g the grain volume, ρ_{bulk} the bulk density, ρ_{grain} the grain density, m_{sat} the saturated weight, m_{sub} the submerged weight, m_{dry} the dry weight and ρ_{fl} the fluid density.

After the water saturation experiments, nitrogen gas (N_2) permeability measurements were carried out, according to the American Petroleum Institute RP40 standard procedure. A Klinkenberg correction was applied to account for the gas slippage effect. The precision of the permeability measurements falls within a range of ±2.5 mD.

3.3 | Mercury injection capillary pressure

A Micromeritics Autopore IV instrument was used to obtain pore throat radii distributions (between 3 nm to 200 μm) in 12 mini-plugs (1.8 cm diameter) that were drilled from the 2.54 cm diameter samples. Mercury injection capillary pressure, described by Purcell (1949), Wardlaw et al. (1988) and Wardlaw and Taylor (1976) is based on the principle that mercury, which is a non-reactive and non-wetting liquid, will only infiltrate the rock's pore network when an external force is applied. The pore throat radii (r) distribution was calculated from mercury capillary pressure curves (P) by means of the mechanical equilibrium equation of Young-Laplace (Equation 6).

$$P = (2\sigma / r) \times \cos(\vartheta) \tag{6}$$

With σ the surface tension and ϑ the contact angle, typically between $90° \leq \vartheta \leq 180°$. The MICP curves are represented (Equation 7) as probability distribution of the pore throats ($f(r)$) versus mercury saturation (S) (Lenormand, 2003).

$$f(r) = P^2 / (2\sigma \times \cos(\vartheta)) \times dS/dP \tag{7}$$

Mercury intrusion determines the amount of mercury injected into the porous solid under various, stepwise increased pressures. The MICP measurements thus produce the amount of pore space behind a given, calculated pore throat size and does not provide measures of pore sizes (Purcell, 1949).

3.4 | Nuclear magnetic resonance

Nuclear magnetic resonance, a non-invasive and non-destructive technique, was applied to measure NMR porosity and PSDs. The PSDs were compared to pore throat size distributions obtained with MICP. In total 42 plugs (2.54 cm diameter), representative of the observed continental spring carbonate facies, were analysed with NMR. Iron oxide bearing samples were not selected for analysis, since NMR signals are very sensitive to the magnetic properties of these minerals. The principles of the NMR method have been described in detail in the literature (Coates et al., 2001; Grunewald & Knight, 2009; Kenyon, 1997; Vincent et al., 2011). In this study NMR transverse relaxometry data of hydrogen nuclei (^1H) were measured at RWTH Aachen University (Institute of Applied Geophysics and Geothermal Energy) using a Carr–Purcell–Meiboom–Gill (CPMG) sequence at a Halbach magnet, generating a 0.22 Tesla static field in a cylindrical region, with a proton resonance frequency of 9.6 MHz. The transverse magnetization decay curve, with transverse magnetization time (M(t); Equation 8), contains important pore network information (Coates et al., 2001; Grunewald & Knight, 2009; Kenyon, 1997).

$$M(t) = M_0 \times e^{-1/T_2} \tag{8}$$

with M_0 the magnitude of the transverse magnetization at the instant the 90° radio frequency pulse ceases.

The transverse relaxation time (T_2) is directly proportional to the volume over surface ratio of the pores (Coates et al., 2001; Nurmi & Standen, 1997; Vincent et al., 2011; Zinszner & Pellerin, 2007). The NMR porosity (Equation 9) was calculated

based on the ratio of the recorded initial amplitude of the rock sample (A_{rs}) and the initial amplitude of a water sample (A_{ws}), with a volume equivalent to that of the rock sample:

$$Ø = A_{rs}/A_{ws} \quad (9)$$

Transformations of the transverse decay magnetization curves were corrected for the bulk relaxation time (T_{2b}) and plotted up to a T_2 of 10,000 ms. A detailed description of this correction can be found in Vincent et al. (2011). A key assumption to interpret T_2 distributions is that hydrogen nuclei are unable to travel between different compartments of the pore network by means of diffusion. If diffusion and mixing between the different compartments does occur, the compartments will behave as coupled systems (Vincent et al., 2011).

3.5 | X-ray computed tomography

Six mini-plugs (7 mm in diameter) were scanned using XCT to generate a 3D rendering of the pore network, and to calibrate NMR T_2 with XCT based pore volume to surface ratios (*V*/*S*). The small sample diameter was necessary to obtain high resolution datasets.

The XCT image acquisition was performed on a Phoenix Nanotom S (GE Inspection Technologies) XCT system. The mini-plugs were mounted on a holder and aligned with the rotation axis of the rotation stage. Tomographic projections were acquired for a 360° rotation angle, with a 0.15° rotation step. X-ray source voltage and current were fixed at 140 kV and 280 μA for all scans. The installed target material consisted of tungsten on CVD synthetic diamond. A 0.3 mm thick copper filter was installed to selectively alter the X-ray spectrum. The hardening of the X-ray beam reduces beam hardening artifacts. The isotropic voxel resolution in all scans was set to 4 μm. With the exposure time set to 500 ms and the fast scan mode activated, a scan time of only 20 min was achieved. Datos|x software was used to reconstruct the XCT scans and to export cross-sectional images. Further processing was done in Matlab and Avizo. First, the sample exterior was subtracted from the images by applying a closing operation and computing the convex hull of the mini-plugs. Next, the mini-plugs were segmented into pores and rock. This was achieved using the hysteresis thresholding function, which returns a binary version of the original greyscale image, based on two predefined thresholds (a weak one, T_w and a strong one, T_s). All voxels with a grey value $<T_w$ are segmented into pores, while voxels with a grey value $>T_s$ are considered rock. All other grey values in between T_w and T_s in the greyscale histogram can become either rock or pore voxels, depending on their 4-way connectivity to neighbouring segmented voxel. The 3D volume renderings of the mini-plugs and their porosity were generated in Avizo.

The surface relaxivity (ρ) was calculated assuming ellipsoidal pores with semi-principal axes *b* and *c* equal to 1 μm and *a* equal to 2 μm, by applying Equation 10 (Coates et al., 2001; Mohnke, 2014) with the T_2 cut-off value (T_{2c}) for microporosity, i.e., 200 ms as defined by Vincent et al. (2011). In the next step, the obtained ρ value was used to calculate the corresponding T_2 relaxation time for the range of *S*/*V* ratios observed in the continental spring carbonate pore networks (Equation 11). The NMR amplitude is strongly dependent on the occurrence frequency of free travel path lengths for protons within pores (Coates et al., 2001). The length of the free travel path was approached in XCT by calculating the distance map for each pore voxel, providing the shortest distance to a rock voxel. The occurrence frequency of the distances is obtained by calculating the frequency distribution of the distance map and is used as a XCT based approximation for the NMR amplitude.

$$\rho = \frac{V}{S} \times \left(\frac{1}{T_{2c}} - \frac{1}{T_{2b}} \right) \quad (10)$$

$$\frac{1}{T_{2(i)}} = \frac{1}{T_{2b}} + \frac{\rho S_{(i)}}{V_{(i)}} \quad (11)$$

4 | RESULTS

4.1 | Facies and lithotypes

A 3D model of the facies distributions throughout the Faber and Ece quarries is given in Figure 2. The main continental spring carbonate facies are described in Table 1. The aggradational sub-horizontal facies (Figure 3A) occurs in the bottom part of the quarries, which is covered by the biostromal reed facies or directly by progradational cascade (Figure 3B) and waterfall (Figure 3C,D) facies slope deposits. Over 40 vol.% of the quarry wall carbonates are composed of cascade facies. Towards the top of the quarries, the dip decreases and biostromal reed facies (Figure 3E) cap the sequence. In the Faber quarry, a marl-conglomerate facies interfingers with the sub-horizontal facies. The conglomerate facies consists of a siliciclastic wedge that thins towards the Ece quarry, where only a thin (±1 m) conglomerate layer can be found. As described by Claes et al. (2015), peloidal, dendritic and phyto-lithotypes dominate the Ece and Faber continental spring carbonates. Peloidal lithotypes, most dominant in the sub-horizontal and cascade facies, consist of amalgamated micritic carbonate spheroids. The peloids (Figure 3F) are typically surrounded by micrite or (micro-)sparite. Dendrite lithotypes consist of micritic dendrites (Figure 3G) or form dendrite crusts (Figure 3H). Micritic dendrites have a characteristic branching nature in their microfabrics. They consist of likely organic-rich, almost opaque micrite, which can be covered by an isopachous (micro-)sparite rim. Phyto-lithotypes

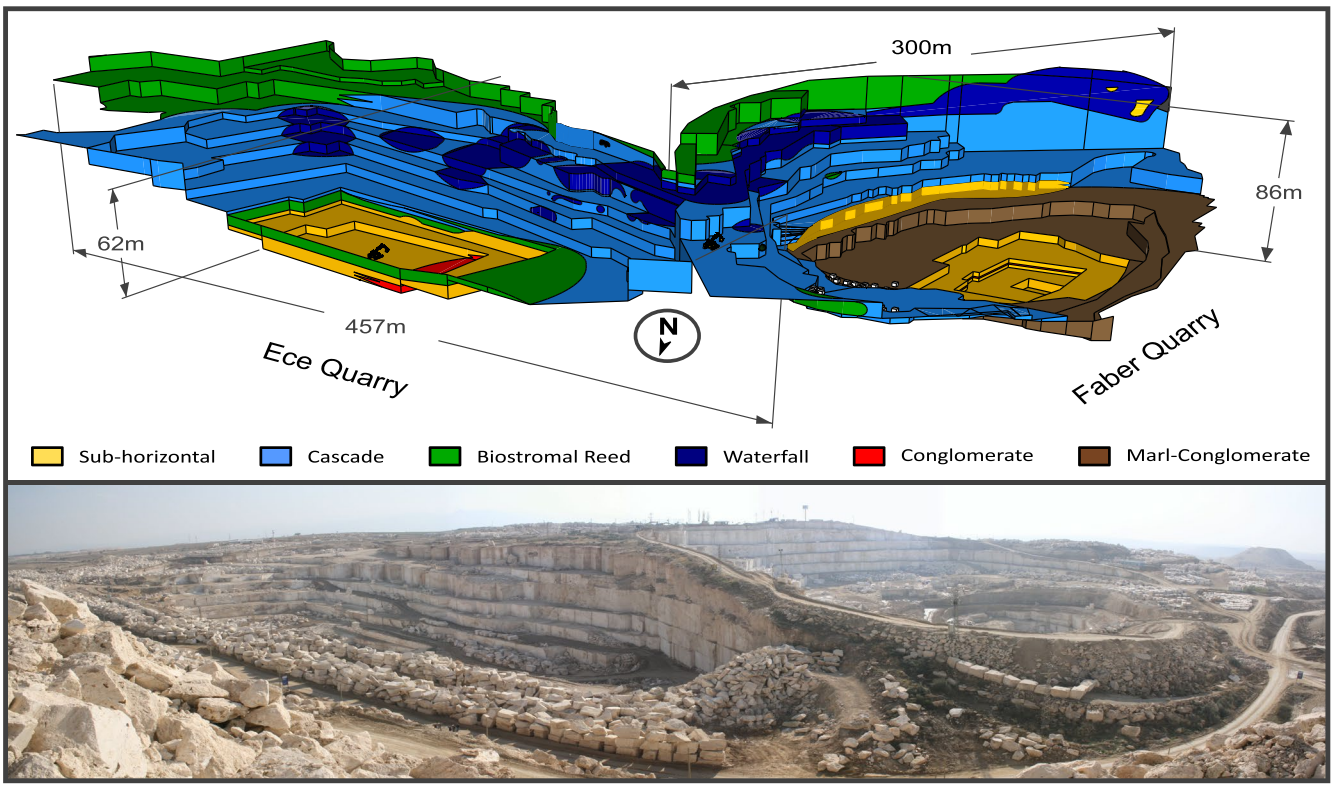

FIGURE 2 The Ece and Faber quarries, 3D model (top) and image (bottom), with matching orientations. The facies distribution throughout the quarries provides insight into the sedimentological history of the system. The 3D model is adapted after Claes et al. (2015)

TABLE 1 Facies and characteristics

Facies	Dominant pore types	Characteristics
Sub-horizontal	Pseudo-fenestral, interlayer	(Sub-)horizontal lamination, with millimetre-scale alternation of white, white/beige and brownish layers. The facies is dominated by the peloidal lithotype. Interpeloidal pores translate into pseudo-fenestral porosity at macro scale (Figure 3A,F)
Biostromal reed	Plant-mouldic	Phyto lithotypes with calcite precipitates and peloids that crenulate around plant casts, resulting in phytoherm low relief topographic mounds (Figure 3E,I,J)
Cascade	Pseudo-fenestral, interlayer, plant-mouldic	Sloping (10–45°) crystalline, dendritic crusts and peloidal lithotypes, which can contain bryophytes and macrophytes (grass and reed; Figure 3B,H)
Waterfall	Framework, plant-mouldic	Steep slopes (>45°), several metres in height. Framework porosity forms between interfingering plants. The plants result in phyto lithotypes (Figure 3C,D). Large shelter cave systems (>20 m^3) occur

(Figure 3I,J), most dominant in the biostromal reed and waterfall facies, are characterised by mouldic pores or plant casts that form the nucleation site on which dendritic micrite grows. The plant casts can appear as sparite cemented moulds. The dendrites are surrounded by (micro-)sparite and peloidal micrite. Depending on the diameter of the plant casts, the phyto-lithotypes are sub-categorised as (from large to small) reed, grass, or bryophyte phyto-lithotypes. Based on

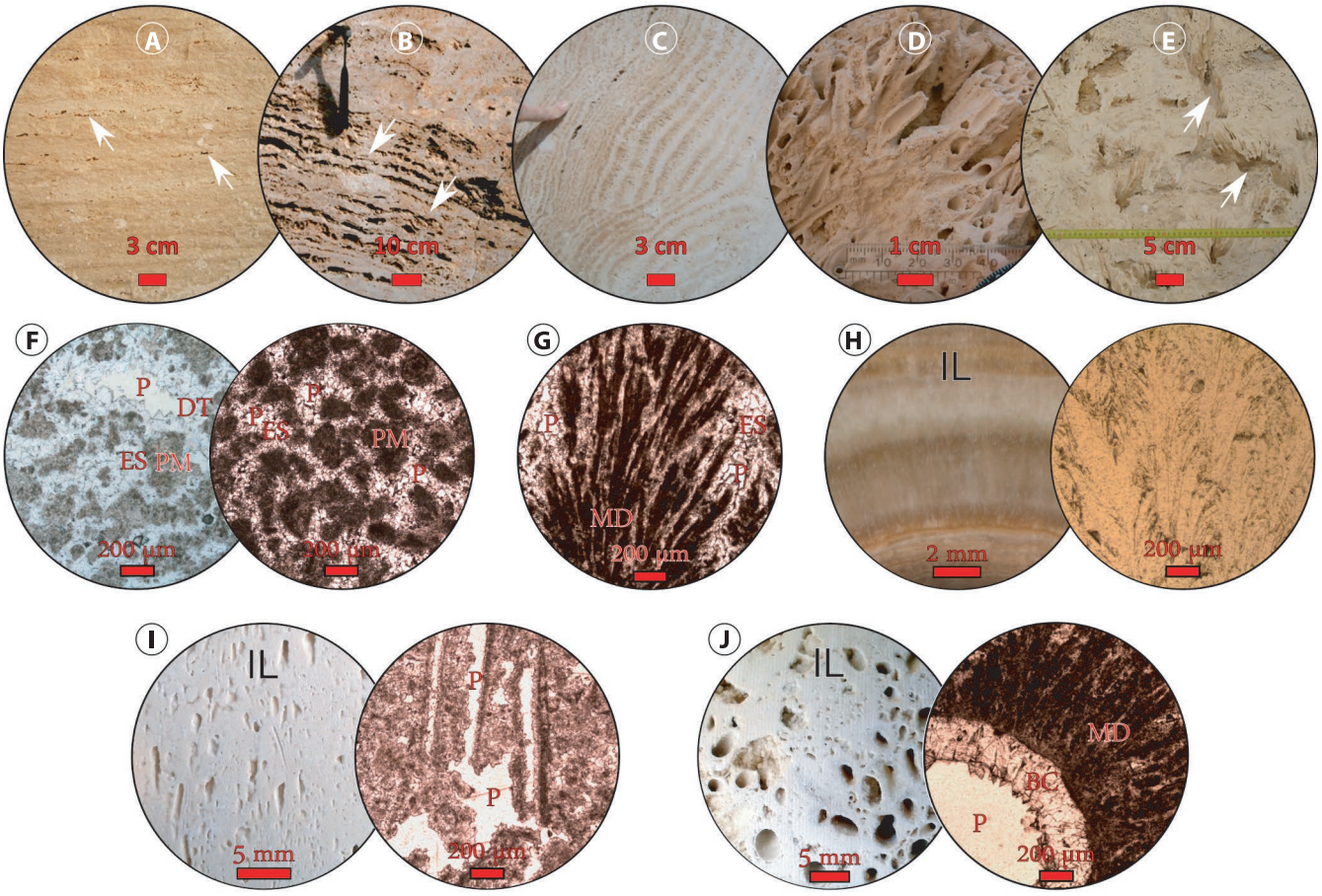

FIGURE 3 Frequently encountered facies and lithotypes in continental spring carbonates in the Ballık area, Turkey. (A) Sub-horizontal facies with pseudo-fenestral porosity, indicated by the arrows. (B) Cascade facies with crenulating crusts lithotypes. The arrows indicate crust layers. (C) Waterfall facies with steeply sloping crust lithotypes. (D) Framework porosity in the waterfall facies. (E) Biostromal reed facies, with reed mouldic pores, indicated by arrows. (F) Peloidal lithotype with peloidal micrite, PM, surrounded with equant spar, ES, and dogtooth spar crystals, DT. Pores, P, occur between the matrix constituents. (G) Dendrite lithotype with the typical occurrence of micritic dendrites, MD. Equant spar, ES, surrounding the dendrite branches. (H) Incident light, IL, and microscopic image of sparitic dendrite crusts. (I) Incident light, IL, and microscopic images of the grass phyto-lithotype. (J) Incident light, IL, and microscopic images of the reed phyto-lithotype. The pores are often reduced by bladed cements, BC, and overgrown with micritic dendrites, MD (figures F, G, H, I, J were adapted after Claes et al., 2015)

the proportion and association of specific lithotypes, the samples can be assigned to the above described sub-horizontal, biostromal reed, cascade and waterfall facies (Table 1). More detailed definitions and descriptions of facies and lithotypes are available in Claes et al. (2015).

4.2 | SEM petrography: Building components and pore type characterisation

Scanning electron microscopy petrography was used to investigate the constituents and pore types of the continental spring carbonates. The peloidal matrix of the continental spring carbonates is formed by micrite, of micron-sized particles, and microsparite crystals, defined here as crystals between 10 and 40 µm (Figure 4A). The micritic appearance can evolve from granular and porous to fitted-fused and tight, resulting in low porosity (Kaczmarek et al., 2015). Porous micrites consist of aggregated small sub-rounded to ovoid and rod-shaped crystals (Figure 4B). The sub-rounded crystals are anhedral to subhedral with point to coalescent contacts (Deville de Periere et al., 2011). The porosity (micron-scale) encountered in between the micrite crystals depends on the size of the crystals, their size sorting and their degree of coalescence (Figure 4B). The crystals in the fitted zones are usually anhedral and coalescent (Figure 4C). In some cases the crystals became fully coalescent, resulting in low porosity, fused micrites.

Microsparite (10–40 µm) surrounds the micrite zones (Figure 4A), appearing as intergrown subhedral crystals (Pedley & Rogerson, 2010; Pentecost, 2005). The morphology of these crystals resembles cuboids with a length-width ratio of 3:1–5:1. Matrix microspar crystals can develop into euhedral calcite rhombs, but these are fairly rare in the examined

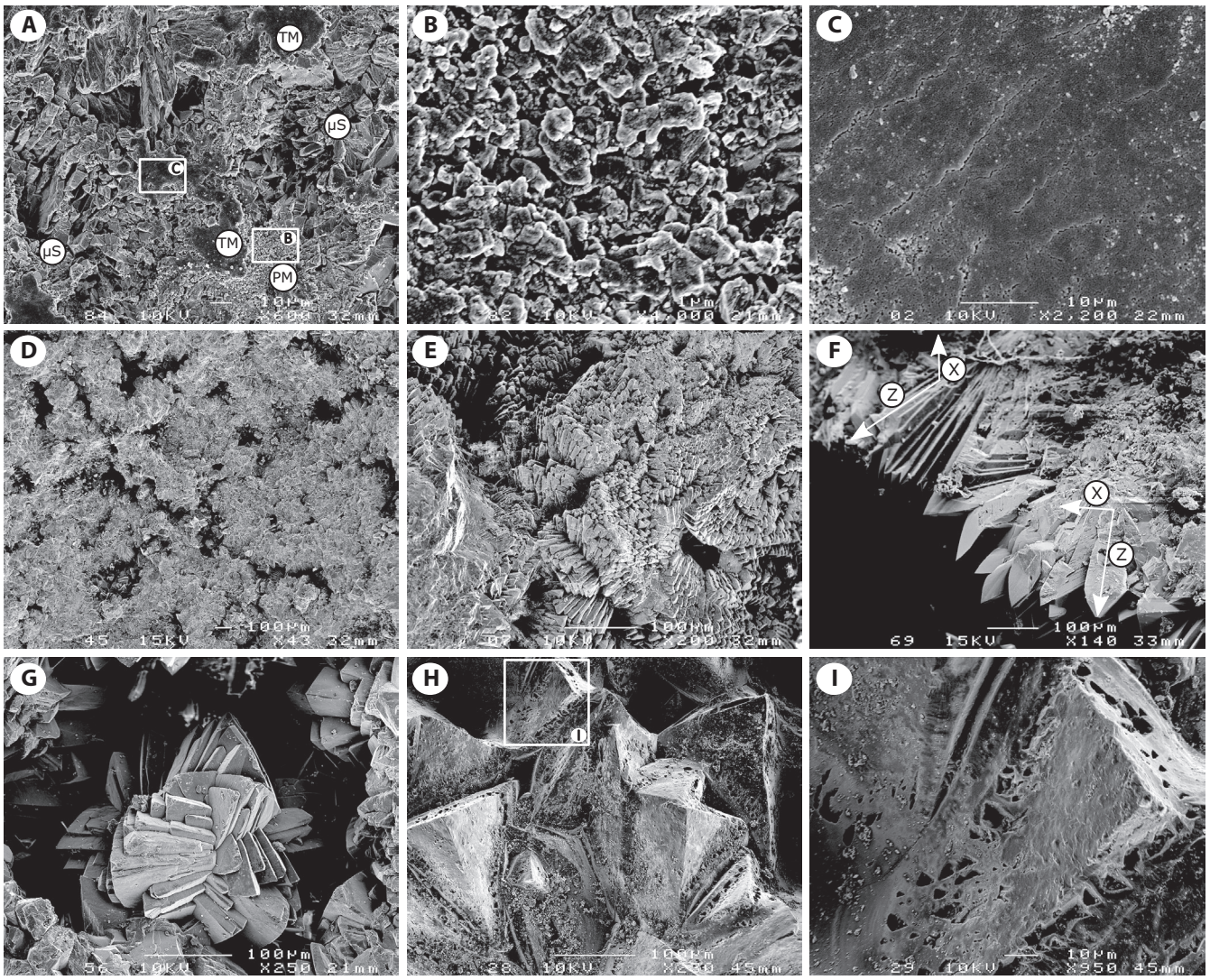

FIGURE 4 Continental spring carbonate SEM photomicrographs. (A) Matrix with granular and porous micrite -PM-, to fitted-fused and tight micrite -TM- and microspar -μS-. (B) Close up view on the porous micrites shown in A. (C) Close up view on the fitted-fused micrites shown in A. (D) Cement-reduced interparticle porosity formed in between peloids by crystal bridging. (E) Sparite field. (F) Isopachous rim of bladed accordion crystals. The *z*-axis of the crystals is perpendicular to the pore wall, with alternating orientation of the *x*-axis. (G) Preferential crystal growth in the pores, resulting in calyx structures. (H) Spar crystals in a sparite field with triangular intracrystalline pores, bound to crystal zonations. (I) Close up view on the triangular intracrystalline porosity inside spar crystals

samples. Intercrystalline pore diameters range from a few up to a few tens of microns. Pore diameters do not exceed crystal sizes. Crystal bridging can result in a well-connected network of large cement-reduced interparticle pores (Figure 4D). The channels in these networks have lengths up to 400 μm and a width of several tens to 100 μm. The channels can develop both horizontally and vertically, mainly determined by the growth direction of the precipitates. Patchy distributed vuggy and mouldic pores of several tens to hundreds of microns are also important contributors to the sample porosity.

Sparite crystals of 40–100 μm occur as isopachous rims along the pore edges, or encrust entire surfaces, resulting in 'sparite fields' (Figure 4E). The bundles of calcite crystals on encrusted surfaces have bladed and spearhead shapes (Özkul et al., 2010). The length axis (*z*-axis) of the sparite blades in the isopachous cement rims is perpendicular to the pore edge, growing towards the pore center. These bladed cements occur in chains with alternating orientations of the *x*-axis, resulting in accordion-like bladed crystals (Figure 4F). The remaining porosity may appear as intercrystalline porosity at SEM scale, but macroscopic and microscopic observations reveal that these pores are in fact cement-reduced vuggy or mouldic porosity (several tens to hundreds of microns in diameter). The sparite crystals are often interlocking and can, in some cases, completely block porosity. Preferential crystal growth inside the pores can result in structures that resemble the calyx of a flower (Figure 4G). Spar crystals can contain

TABLE 2 Petrophysical and facies properties of the samples

Sample	Orientation	Facies	Lithotype	ρ_{bulk} (g/cc)	ρ_{grain} (g/cc)	Archi Ø (%)	NMR Ø (%)	K_{kl} (mD)	Radii (μm)
EC10HC002	Vertical	Sub-horizontal	Peloidal	2.55	2.61	3.8	2.9	0.010	—
EC10HC004	Vertical	Sub-horizontal	Peloidal	2.48	2.61	8.4	5.4	0.010	—
EC10HC007	Vertical	Biostromal reed	Peloid-Grass	2.47	2.63	10.1	7.1	0.018	—
EC10HC012	Vertical	Cascade	Grass	2.53	2.65	7.1	5	0.010	—
EC10HC023	Vertical	Waterfall	Reed	2.32	2.61	18.3	15.7	1,265	—
EC10HC027	Vertical	Cascade	Reed	2.26	2.62	22.5	13.6	2.6	—
EC10HC030	Vertical	Cascade	Grass	2.42	2.66	14.8	8.7	13.7	—
EC10HC041	Vertical	Cascade	Peloidal	2.42	2.67	15.0	9.7	250	16
EC10HC047	Vertical	Cascade	Grass	2.53	2.65	7.7	6	0.006	—
FA10JS002	Vertical	Cascade	Grass	2.49	2.61	7.5	4.2	0.349	1.5
FA10JS005	Vertical	Cascade	Peloid-Grass	2.44	2.60	9.9	4.7	682	18
FA10JS010	Vertical	Waterfall	Grass	2.45	2.60	9.1	6.3	178	—
FA10JS021	Vertical	Sub-horizontal	Peloidal	2.50	2.60	6.2	5.6	0.009	—
FA10JS028	Vertical	Sub-horizontal	Peloidal	2.50	2.64	8.4	6.3	1.7	—
FA10JS037	Vertical	Sub-horizontal	Peloidal	2.41	2.65	14.3	10.5	34.7	11
FA10JS039	Vertical	Biostromal reed	Reed	2.54	2.64	6.1	4.1	0.004	—
FA10JS047	Vertical	Cascade	Peloidal-Grass	2.59	2.65	4.0	2.4	0.010	0.7
FA10JS053	Vertical	Cascade	Reed	2.31	2.62	18.9	15.2	0.803	—
FA10JS056	Vertical	Waterfall	Reed	2.22	2.62	24.3	17.2	0.114	—
FA10JS104	Horizontal	Sub-horizontal	Peloidal	2.55	2.63	5.1	3.3	10.6	—
FA10JS141	Horizontal	Waterfall	Reed	2.28	2.61	20.8	10.4	0.029	—
FA10JS142	Vertical	Waterfall	Reed	2.34	2.57	14.8	7.6	0.044	19
FA10JS143	Horizontal	Biostromal reed	Reed	2.43	2.59	10.4	8.2	0.168	2
FA10JS144	Vertical	Biostromal reed	Grass	2.42	2.58	10.2	5.3	0.025	—
FA10JS145	Horizontal	Biostromal reed	Reed	2.40	2.64	14.2	11.3	0.028	—
FA10JS146	Horizontal	Waterfall	Grass	2.29	2.66	21.9	14.2	0.142	6.5
FA10JS148	Vertical	Waterfall	Bryophyte	2.36	2.64	17.0	10.9	2,558	—
FA10JS149	Horizontal	Biostromal reed	Grass	2.49	2.63	8.5	5.7	0.410	—
FA10JS150	Horizontal	Biostromal reed	Bryophyte	2.52	2.64	7.2	4.7	1.4	0.5
FA10JS151	Vertical	Biostromal reed	Grass	2.49	2.69	11.4	9.9	0.220	—
FA10JS153	Vertical	Biostromal reed	Grass	2.34	2.63	17.9	9	0.076	—
FA10JS154	Horizontal	Biostromal reed	Reed	2.41	2.64	13.6	8.3	4.7	1.5
FA10JS155	Horizontal	Biostromal reed	Reed	2.39	2.64	15.5	10.2	3,675	—
FA10JS156	Horizontal	Biostromal reed	Grass	2.37	2.63	16.3	12	1.7	1.5
FA10JS157	Horizontal	Biostromal reed	Reed	2.52	2.65	8.0	5.7	1.0	—
FA10JS158	Horizontal	Sub-horizontal	Peloidal	2.50	2.65	8.8	4.4	0.092	—
FA10JS160	Vertical	Sub-horizontal	Dendrite crust	2.50	2.62	7.8	5.6	22	—
FA10JS161	Horizontal	Cascade	Peloidal	2.45	2.64	11.6	6.8	18.7	8.5
FA10JS163	Horizontal	Cascade	Grass	2.45	2.62	10.3	6.9	0.124	—
FA10JS164	Vertical	Cascade	Reed	2.54	2.61	4.2	3.6	0.008	—

Note: ρ_{bulk}: Bulk density; ρ_{grain}: Grain density; Archi Ø: Archimedes porosity; NMR Ø: NMR porosity; K_{kl}: Klinkenberg permeability; MICP based average pore throat radii (radii). The listed lithotypes correspond to the visually defined dominant lithotypes in each plug.

intracrystalline porosity of a few microns in diameter. For example, samples taken near the top of the quarries contain spar crystals with triangular intracrystalline pores (possibly due to dissolution), arranged according to the crystal growth zonation (Figure 4H,I).

4.3 | Petrophysical measurements

The results of the laboratory measurements, i.e., the bulk density, grain density, Archimedes porosity (Archimedes Ø), NMR porosity (NMR Ø), permeability and average pore throat radii (radii) of the specimens are given in Table 2. The bulk density of the samples ranges between 2.22 and 2.59 g/cm^3. This is in agreement with earlier reported bulk densities for continental, calcareous spring carbonates (Soete et al., 2015).

Table 2 shows Archimedes porosities varying from 2.7% to 24.3%. The grain densities, ranging from 2.57 to 2.69 g/cm^3, are somewhat lower than typical calcites, that vary around 2.71 g/cm^3 (Mavko et al., 2009). Lower than expected grain densities in continental spring carbonates are due to the presence of unaccounted low density impurities, e.g., water, air, organic matter, or magnesium, sulphur or sulphate replacements in the crystal lattice (Claes et al., 2020). Isolated micropores, which were not reached during the porosity analyses also lower the grain density of the sample.

The porosity and permeability of the vertical and horizontal continental spring carbonate plugs are shown in a cross-plot (Figure 5). Petrophysical heterogeneity is observed, with differences in porosity that exceed 20% and permeabilities ranging between 0.004 and *ca* 4,000 mD. Some of the highest porosities resulted in permeabilities below 1 mD, while samples < 10% porosity frequently yielded permeabilities > 1 mD and even up to 900 mD.

The porosity and permeability statistics for the horizontally and vertically oriented samples respectively, are given in Table 3. The calculated properties, i.e., *SD*, sample variance and ranges, are of the same order of magnitude for horizontally and vertically oriented plugs. Samples from the sub-horizontal facies yielded somewhat higher permeabilities in the horizontal direction, while for the other facies no distinct trends for horizontal or vertical directions were observed. In general, no straightforward relationships between porosity, permeability and facies types were observed.

4.4 | MICP and NMR PSDs

A coupled investigation with MICP and NMR was applied to verify and interpret the obtained distributions of the samples (Giesche, 2006; Yao & Liu, 2012). Nuclear magnetic resonance porosity is calculated based on the initial amplitude in the decay curve (Figure 6A). The latter corresponds to the decay signal of the bulk of hydrogen nuclei in the saturated sample and reflects its saturated porosity. The NMR porosity, ranging between 1.7% and 17.2%, was plotted against the Archimedes porosity and yields a linear determination coefficient of 0.87 (Figure 6B). Despite the linear correlation, the NMR porosity is generally lower (on average by 3.9%) than the Archimedes porosity (Figure 6B).

The MICP distributions are given in Figure 7A and illustrates that a continuum of pores with throat radii (r) of approximately 1–200 μm is present in all continental spring

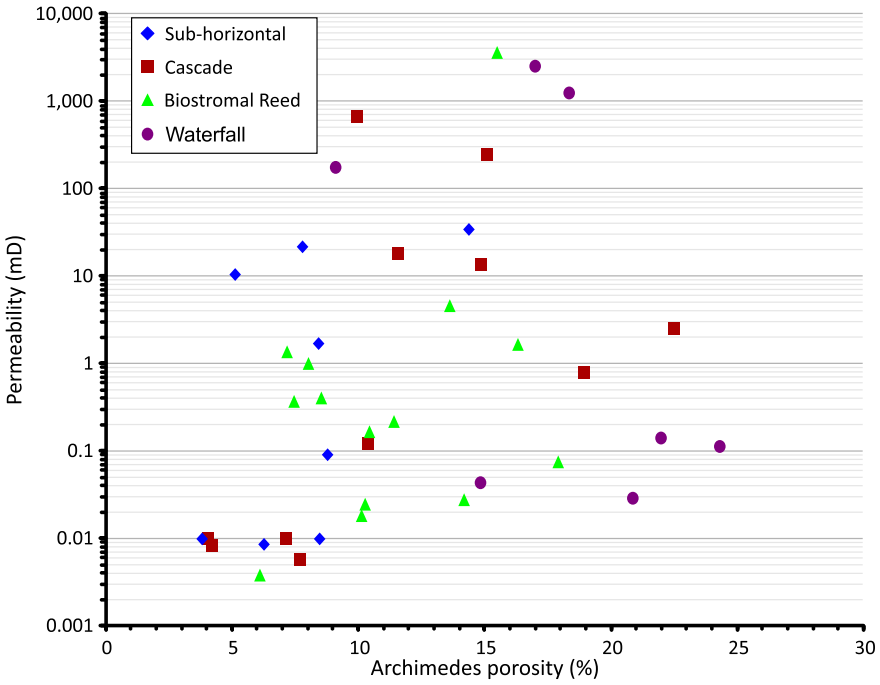

FIGURE 5 Porosity–permeability cross plot for the studied continental spring carbonates from the sub-horizontal, biostromal reed, cascade and waterfall facies

carbonate samples. These pores are defined in this study as mesopores (r = 1–15 μm) and macropores (r > 15 μm), in agreement with Vincent et al. (2011). The log mean of the pore throat radii is 21 μm and the mode of the frequency distribution is 20 μm. The latter pore throat radii sizes fit well with the expected sizes for the connections between mesopores and macropores based on SEM observations. Samples with a bimodal distribution contain additional pores with throat radii in the nanometre domain, defined here, in agreement with Schlumberger Limited (2015) and Zinszner and Pellerin (2007), as micropores (r < 1 μm). The mode of the secondary peak, 20 nm, likely corresponds to the connection between the micropores. The NMR T_2 distributions, assembled in Figure 7B, allow assessment of whether the sample set collected from different facies types follows facies specific patterns. The bulk relaxation time of the water reference sample was 3,250 ms. The corrected NMR distributions were plotted up to 10,000 ms. Some NMR curves partly exceed this value, and this is likely caused by noise associated with the presence of very larger pores, influencing the tail of the measured NMR transient (Vincent et al., 2011).

The PSD curves are unimodal or bimodal. The integration of the MICP and NMR data allows subdivision into three categories without taking petrographical characteristics into account:

1. Unimodal samples (red curves in Figure 7). These samples present one peak in MICP (r = 1–200 μm) and NMR (T_2 values between 100–200 and 10,000 ms).
2. Bimodal samples (blue curves in Figure 7). For bimodal samples a secondary peak occurs left of the primary peak both in MICP (r = 3 nm–1 μm) and NMR (T_2 = 10–200 ms).
3. Atypical samples (yellow curves in Figure 7). Samples for which the NMR and MICP distributions present a different modality. The MICP distributions are bimodal, while NMR distributions are unimodal. The NMR PSD is, however, different from unimodal samples, since it rises from T_2 relaxation times of 10 ms instead of 200 ms. The atypical distribution can contain a strong shoulder towards shorter relaxation times.

Typical examples for each of the above mentioned groups are given in Figure 8. In the unimodal group, i.e., mesoporous and macroporous samples (Figure 8A), the MICP distribution demonstrates that pores with throat radii below 1 μm hardly occur. The corresponding NMR T_2 distribution curve starts off at approximately 200 ms, 200 ms T_2-time is therefore considered the upper threshold for microporosity. Vincent et al. (2011) and Brigaud et al. (2014) defined a NMR T_2 cut-off value in marine carbonates for microporosity that also corresponds with the

TABLE 3 Horizontal and vertical porosity and permeability statistics

Orientation of the plug	Horizontal		Vertical	
Number of plugs	15		25	
Measured properties	Archi Ø (%)	K_{kl} (mD)	Archi Ø (%)	K_{kl} (mD)
Minimum	5.1	0.028	3.8	0.004
Maximum	21.9	3,675	24.3	2,558
Mean	12.3	265	11.5	193
SD	5.0	981	5.7	556
Sample variance	25.3	963,071	32.8	309,568
Range	16.9	3,675	20.5	2,558

Note: Archi Ø: Archimedes porosity; K_{kl}: Klinkenberg permeability.

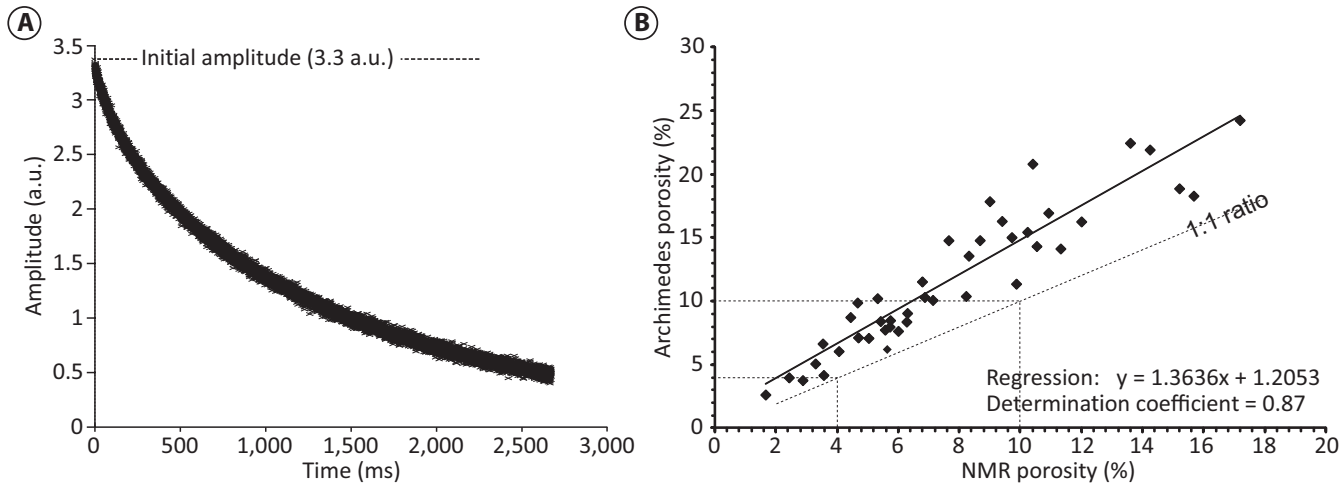

FIGURE 6 (A) Example of an NMR magnetization decay curve, the initial amplitude is given in arbitrary units (a.u.) and used to calculate NMR porosity. (B) Cross plot of Archimedes and NMR porosity

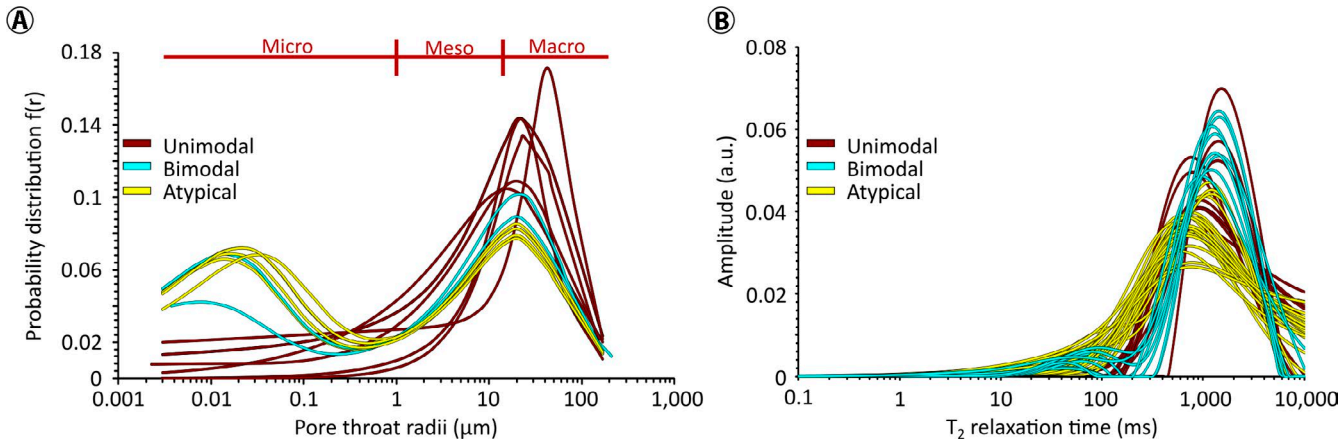

FIGURE 7 (A) MICP pore size distributions. The samples have an unimodal or bimodal distribution. The main peak of the distributions is found between 1 and 200 μm, bimodal samples have a secondary peak, which is located between 3 nm (the lower limit of the technique) and 1 μm. (B) NMR *T*2 distributions. Unimodal, bimodal and atypical (bimodal in MICP, but not in NMR) NMR curves are observed

200 ms T_2 cut-off that is applied here. A similar cut-off is deduced in continental spring carbonates in De Boever et al. (2016).

Continental spring carbonates with bimodal distributions (Figure 8B) contain micropores, with throat radii smaller than 1 μm, as well as mesopores and macropores. The presence of the micropores is imaged within the NMR T_2 distribution, where a new peak appears at relaxation times below 200 ms. The atypical samples (Figure 8C) contain bimodal MICP distributions, but unimodal NMR distributions. In contrast to the other unimodal distributions, however, the NMR distribution curves rise from T_2 relaxation times of 10 ms instead of 200 ms. The atypical distribution can contain a strong shoulder towards shorter relaxation times. Micropores, mesopores and macropores are present in the pore network of the atypical samples. Multimodal curves are indicative of the presence of multiple pore compartments, of which two were recognised in the continental spring carbonates by means of the bimodal MICP distributions. The first compartment, present in all samples, contains mesopores and macropores. In a number of samples a second compartment can be recognised that consists of micropores. When bimodal (Figure 8B) and atypical (Figure 8C) NMR distributions are compared, a shift in the maximal amplitude (1,500–1,000 ms), and in the T_2 log-mean ($T_{2(lm)}$, from 967 to 762 ms) is observed (Figure 8).

Unimodal, bimodal and atypical PSD types are, as opposed to the facies types, associated with distinct porosity—permeability characteristics (Figure 9A). Unimodal samples have porosities below 16%, but permeabilities reaching 1,000 mD. The atypical samples follow a similar porosity–permeability trend, but permeabilities of over 3,500 mD are present. Bimodal samples generally possess high porosities (mainly >15%–25%), but generally have reduced permeabilities (mainly < 5 mD). In Figure 9B, the porosity—permeability plot is given as a function of the dominant lithotype. Almost all atypical and bimodal distributions are present in samples dominated by phyto-lithotypes, e.g., reed, grass and bryophyte phyto-lithotypes. Unimodal samples relate to peloidal lithotypes. One cascade sample, with dendrite crusts as dominant lithotype, showed atypical behaviour. In agreement with Melim et al. (2001), the porosity—permeability relationship does not relate well with facies types, but does relate with PSD types, which in turn depend on the dominant lithotype in a sample.

4.5 | Pore typing

Mesopores and macropores are present in all examined continental spring carbonate samples. Petrography showed that pore types that contribute to the macroporosity (r > 15 μm) consist of intercrystalline, vuggy, mouldic and cement-reduced interparticle porosity.

Unimodal samples are dominated by peloidal lithotypes. Polarized light microscopy images of this (Figure 10A) show dark brown, almost opaque micritic carbonate peloids which are typically surrounded by light brown micrite and transparent sparite. The mesoporous nature of the peloidal micrite is evidenced by its fluorescent properties in FM. The sparites are non-fluorescent under fluorescent incident light (Figure 10B). The fluorescent resin penetrated macropores, but also the micritic zones, proving they contain mesoporosity (r = 1–15 μm). The sparites, however, almost completely lack porosity. The intramicrite porosity, i.e., pores between micrite crystals, inside micritic zones depends on the size and coalescence of the micrite crystals.

Together with intracrystal and intercrystal pore types, intramicrite porosity provides the mesoporosity, the smallest pores present in the unimodal samples (T_2 > 200 ms, Figure 10C). Micritic fabrics, with intramicrite porosity cover large areas in the sample and often enclose macropores as an envelope. Dendrite lithotypes can display

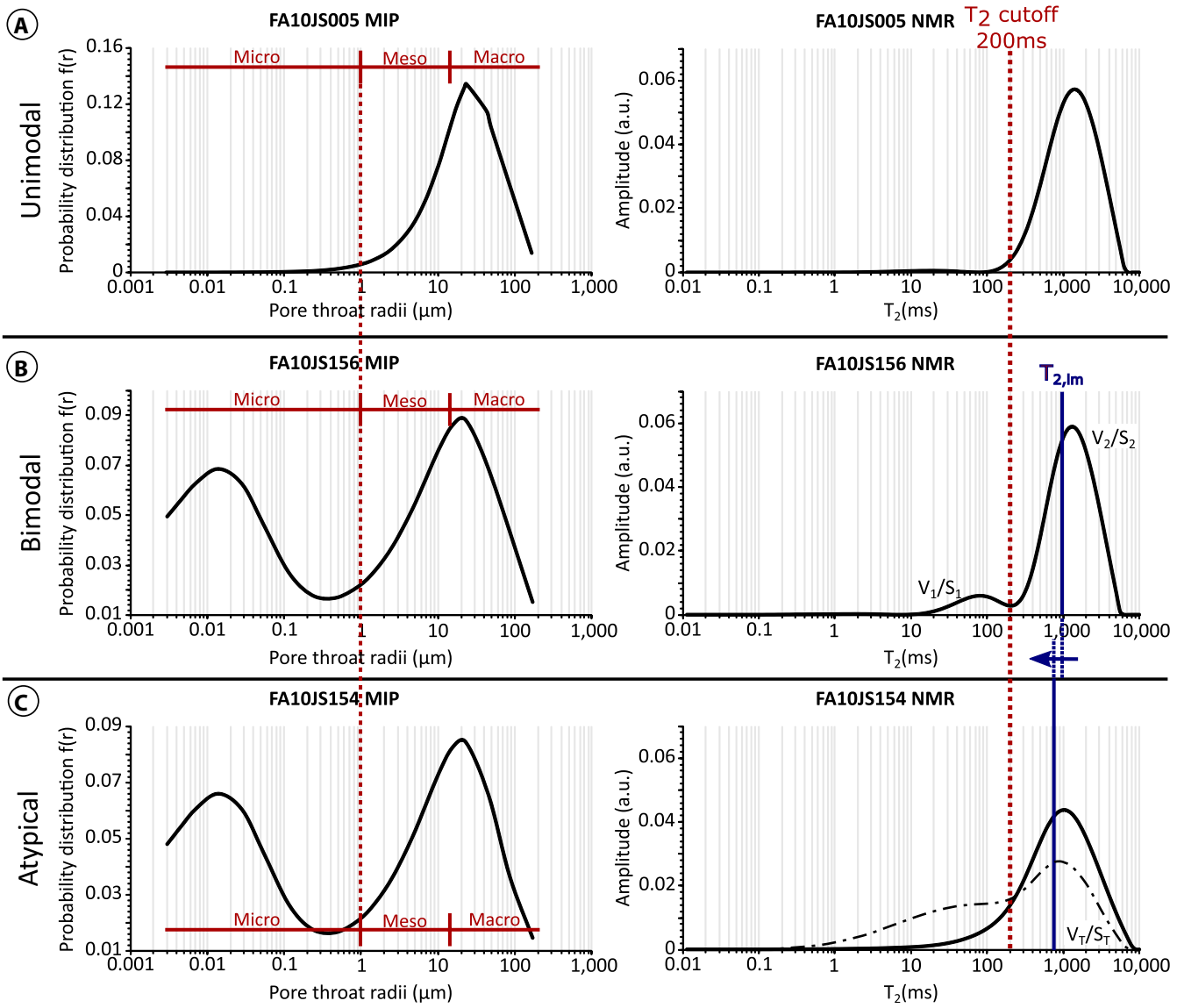

FIGURE 8 Comparison between MICP pore throat radii and NMR *T*2 distributions. (A) Meso- and macroporous sample FA10JS005, (B) Micro-, meso- and macroporous sample FA10JS156. Two compartments are observed, characterised by a specific *V*/*S* ratio (*V*1/*S*1 and *V*2/*S*2). (C) Atypical micro- to macroporous sample with a bimodal MICP and unimodal NMR *T*2 distribution, sample FA10JS154. Only one compartment can be recognised in NMR and is described by VT/ST, the total volume and surface of both compartments. A shift in the *T*2 log-mean towards shorter relaxation time is observed. The dashed line represents an atypical distribution with a distinct shoulder towards shorter relaxation times

unimodal NMR distributions, but less typically than peloidal lithotypes.

Microscopy of atypical and bimodal samples revealed a strong presence of phyto moulds, overgrown by dendritic structures, for which the original plant structures functioned as a nucleation site (Figure 10D). In between dendrite branches and in between the dendrites themselves, pore spaces are to variable degrees occupied by (micro)spar crystals. The SEM imaging demonstrated that micropores ($r < 1$ µm) can be found all over the dendritic branching structures (Figure 10E). The micropores in these microporous micritic dendrites are aligned and occur as elongated objects along the growth direction of the dendrites. The microporous nature of the dendrites is also observed in CT, where dendritic crusts occur as low tomodensity areas, i.e., with limited attenuation compared to rock voxels, but higher attenuation than pore voxels, around spar cemented mouldic pores (Figure 10F). The low tomodensity areas are indicative of pore sizes close to, or below the scan resolution and as such, it is not possible to label individual micropore objects. A notable difference between bimodal and atypical PSD types is that plant mouldic pores appeared cement reduced (Figure 10G,H) in bimodal distributions (Figure 10I), whereas in atypical distributions (Figure 10K), those mouldic pores appeared as non-sealed systems, devoid of calcite cements (Figure 10J). A summary of the pore types and

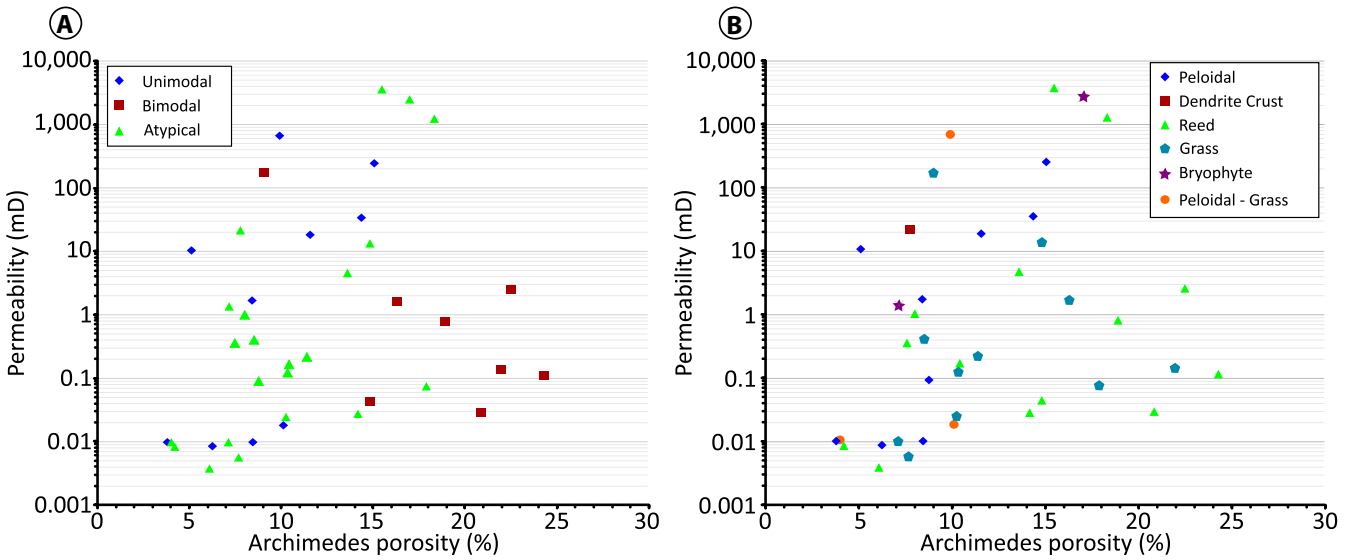

FIGURE 9 (A) Unimodal, bimodal and atypical NMR PSD types and (B) dominant lithotypes in the porosity–permeability cross plot

their pore throat sizes, encountered during SEM and petrography, are given alongside a representative MICP distribution in Figure 11.

4.6 | T_2 log-mean and its relationship to porosity, permeability and pore throat sizes

The logarithmic mean of the transverse relaxation time ($T_{2(\mathrm{lm})}$) of each NMR measurement was calculated and compared to petrophysical parameters such as porosity, permeability and average pore throat radii size from MICP analysis. $T_{2(\mathrm{lm})}$ values well above 200 ms are indicative of large macropore to micropore ratios. Only a few samples yield a $T_{2(\mathrm{lm})}$ closer to, or below 200 ms. For these samples the macropore to micropore ratio decreases and micropores have a stronger influence on the NMR distribution, as earlier described by Brigaud et al. (2014). Plotting the $T_{2(\mathrm{lm})}$ against porosity (Figure 12A) and permeability (Figure 12B) shows that pore body size does not relate to porosity, nor to permeability. In continental spring carbonates, like for all other carbonates, the porosity is independent of pore body size, for example samples with larger pores ($T_{2(\mathrm{lm})}$ = 1,200 ms), but also samples with large volumes of smaller pores ($T_{2(\mathrm{lm})}$ = 800 ms), can result in high porosities. Porosity is derived from the total volume of fluid that can be injected in a sample, while permeability is dependent on the connectivity between these pores and Figure 12B illustrates how larger pores do not necessarily guarantee better connections.

A linear correlation (determination coefficient of 0.61 for 12 samples measured with both NMR and MICP) was found between average pore throat radii sizes and $T_{2(\mathrm{lm})}$ (Figure 12C). The average pore throat radii sizes for the different samples, measured in the MICP analyses, ranged between approximately 0 and 20 µm. Samples with a larger average pore throat radius were associated with a higher $T_{2(\mathrm{lm})}$. In other words MICP pore throat sizes and NMR pore body sizes are related, as also visualised based on SEM observations. However, deviations of 200 ms $T_{2(\mathrm{lm})}$ from the regression line occur. Finally, an exponential relationship (determination coefficient of 0.70 for 11 samples with one outlier) is observed between average pore throat size and permeability (Figure 12D). The permeability is dependent on the connections between the pore bodies. One outlier is indicated in Figure 12D and corresponds to a macroporous sample (FA10JS142, 14.8% porosity), which yields low permeability (0.04 mD) due to the presence of a thick cement rim that almost fully blocks the pores.

An attempt was made to estimate permeability based on NMR measurements by applying the SDR model (Anferova et al., 2007; Coates et al., 2001). The SDR modelled permeability did not match the measured permeability. Westphal et al. (2005) discussed the impact of pore-types on the calibration constants used in the equations. It is expected that the pore type variability within a plug sample of the here studied continental spring carbonates prohibits defining a suitable calibration constant. More detailed information can be found in Soete (2016).

4.7 | Calibration of NMR and CT

This section investigates the extent to which the XCT approach provides representative output for the porous network in continental spring carbonates, and whether unresolved porosity could drastically affect the obtained digital pore network models. Nuclear Magnetic Resonance and XCT PSDs, calculated for surface relaxivities of 1.8 µm/s, are compared in Figure 13.

The calculated T_2 distributions from XCT only represent a part of the NMR distribution, as pores smaller than the

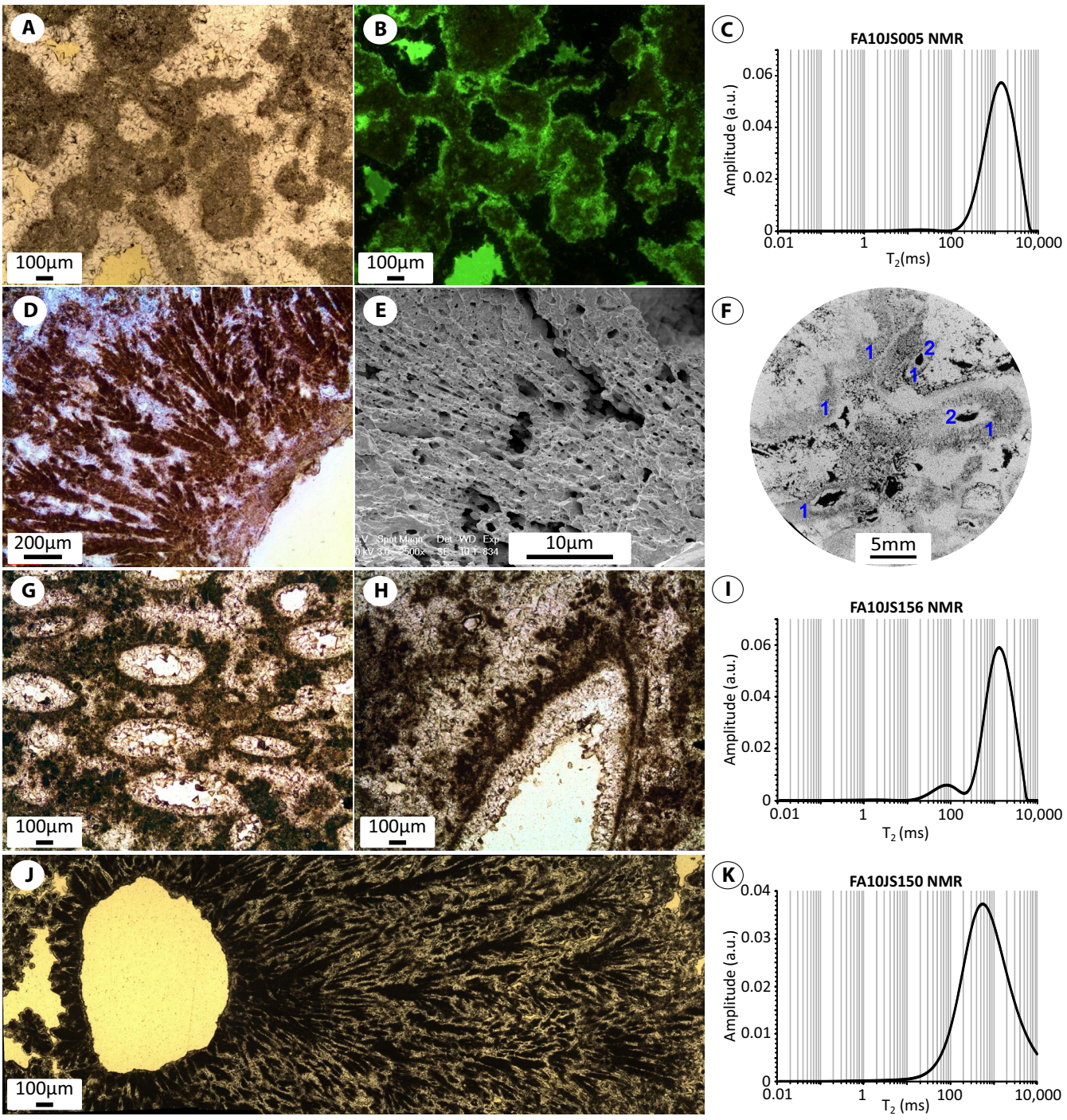

FIGURE 10 (A) Polarized light micrscopy (PLM) image of the peloidal lithotype, with dark micrite cloths and light brown micrite in between white sparite crystals. (B) Fluorescence Microscopy (FM) image of 10A, with pores and micritic zones that show fluorescent properties. Sparites appear as non-porous. (C) Unimodal *T*2 curve, typical for peloidal lithotypes. (D) PLM image of dendritic fabrics growing on the edge of a reed mouldic pore. (E) SEM image with microporous dendrites. (F) XCT image of dendrites (1) in the matrix of the sample or overgrowing cement reduced moulds (2). (G, H) PLM image of dendritic structures, nucleating on cement reduced mouldic pores. (I) Bimodal *T*2 curve, typical for micropores in dendrites that are isolated from meso- and macropores by isopachous sparite rims. (J) PLM image of dendrites that are in direct contact with the reed mouldic pore on which they grow. (K) Atypical *T*2 curve, formed when micropores in dendritic structures are able to communicate with meso- and macropores

maximal NMR amplitude ($T_2 < 700$ ms) are missing. The calculated T_2 distribution ranges between approximately 700 and 2,800 ms. The upper limit of the XCT PSD is defined by the bulk relaxation time, the lower limit by the XCT scan resolution. The porosity, calculated from segmented XCT images is compared to NMR porosity (Table 4). Despite the difference in

sample volume over which NMR and XCT porosity are measured, it can be deduced that XCT porosity is generally lower than NMR porosity, with the exception of sample FA10JS047.

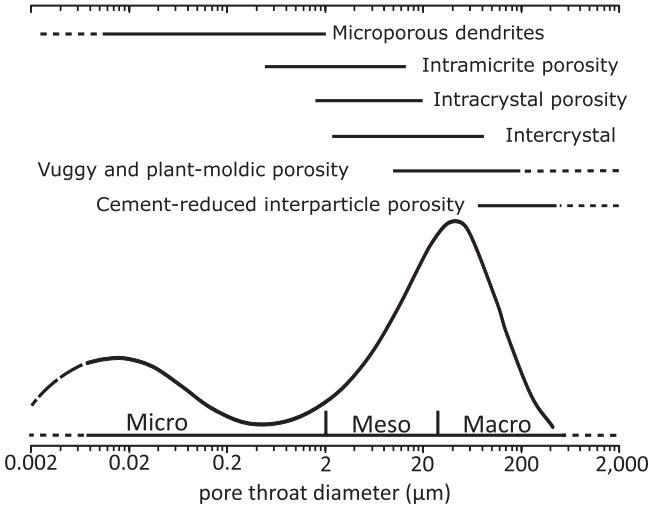

FIGURE 11 Example of an MICP pore size distribution curve. Added on top are the pore throat radii ranges of the pore types observed in the continental spring carbonates

The average pore volume (AV), average surface area (AS) and the ratio of these two (AS/AV) are also given in Table 4. AS/AV is a sample average of the surface over volume ratios (*S*/*V*) that were calculated for each pore and used in the XCT T_2 estimation. The NMR distributions of samples with smaller pores and lower porosity (FA10JS154 with an average pore volume of 97,002 μm^3 and a porosity of 8.3%, Figure 13A) correspond to more condensed XCT PSD profiles, with estimated T_2-times below 2,600 ms and lower estimated amplitudes. Samples with larger pores and higher porosity (FA10JS155, with an average pore volume of 386,193 μm^3 and a porosity of 10.5%, Figure 13B) were characterised by longer XCT PSD profiles, with estimated T_2-times up to 3,000 ms, and higher amplitudes. Figure 14A,B show orthogonal slices and a partial 3D rendering of the pore networks of the samples shown in Figure 13A,B, respectively. The XCT images illustrate the differences between the PSDs for samples dominated by the bryophyte or reed phyto-lithotype, respectively. Many small bryophyte mouldic pores (Figure 14A) are present in the former, while fewer but larger reed mouldic and vuggy pores dominate the latter (Figure 14B).

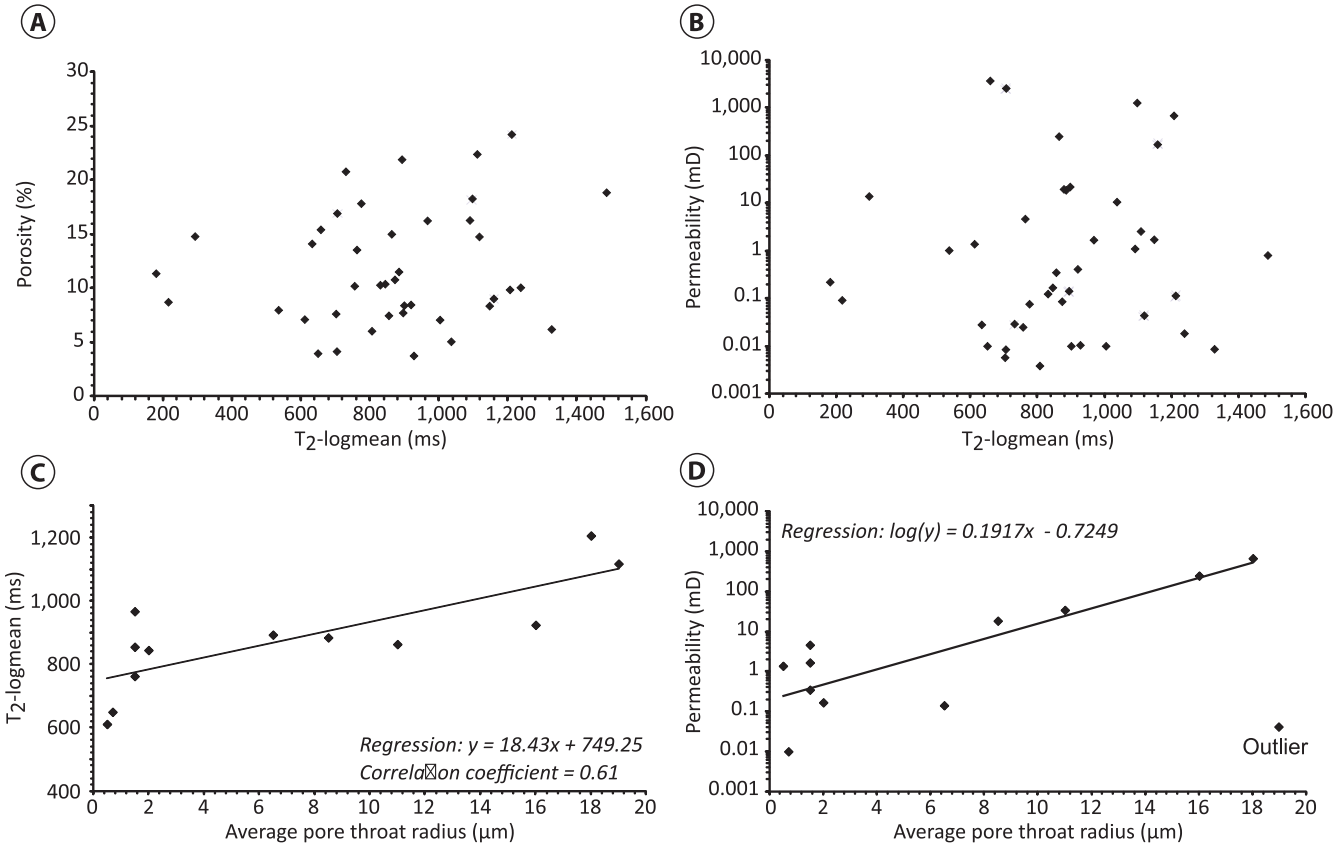

FIGURE 12 *T*2 log-mean from NMR versus the logarithmic mean of the pore throat radii from MICP in scatter plots with porosity and permeability. (A) *T*2 log-mean versus porosity with strongly scattered data. (B) *T*2 log-mean versus permeability. No relationship between both parameters is observed. (C) Average pore throat radius versus *T*2 log-mean. Pore throat and pore body size yield a linear correlation. (D) Average pore throat radius versus permeability, with a linear correlation between both parameters and one outlier

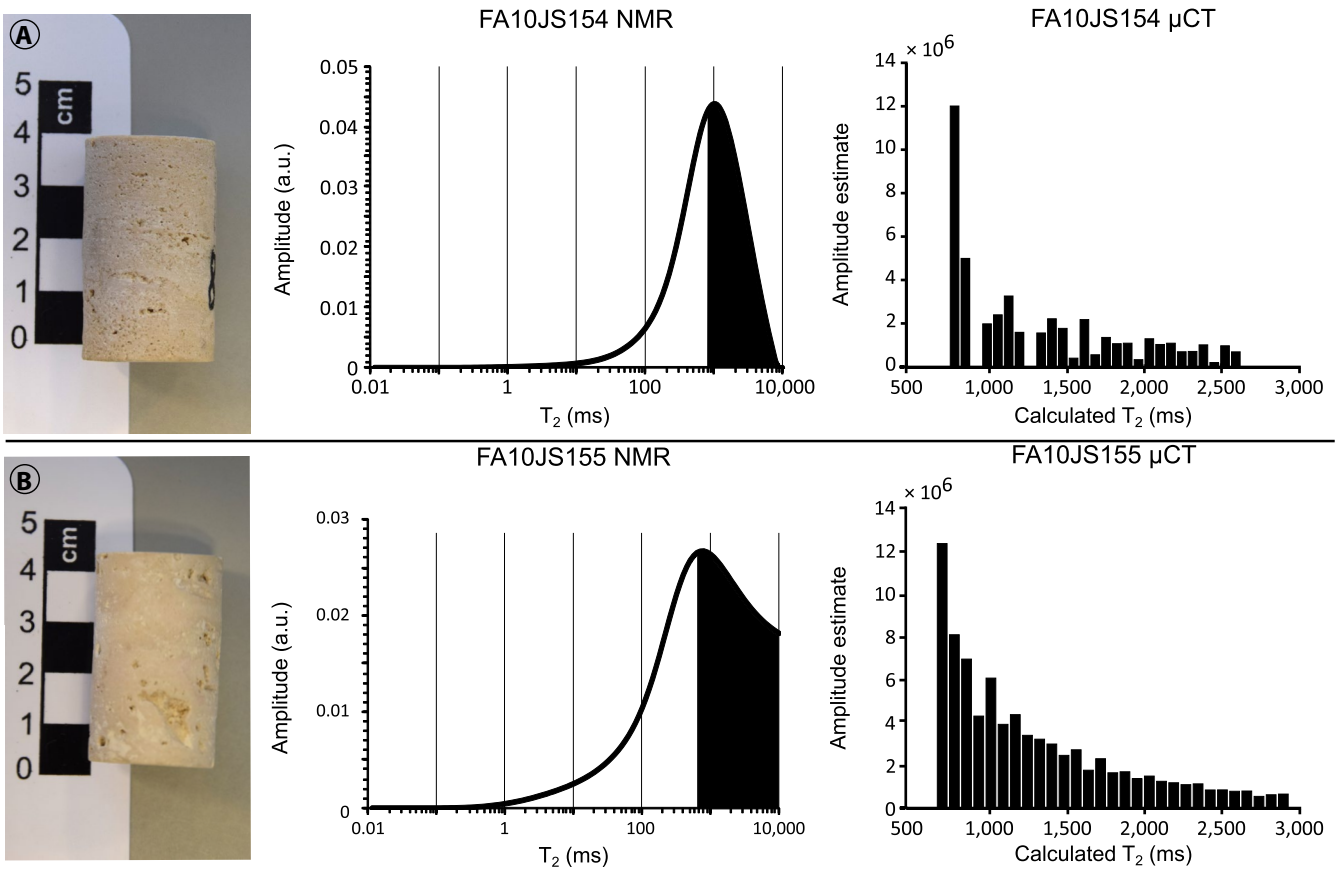

FIGURE 13 Plug samples and their respective NMR and XCT *T*2 distributions. (A) FA10JS154 with XCT calculated *T*2 values from 800 ms up to 2,600 ms. (B) FA10JS155, with a NMR distribution with a strong shoulder towards 10,000 ms. XCT *T*2-times up to 3,000 ms were calculated

TABLE 4 NMR and XCT porosity

Sample	NMR Ø (%)	XCT Ø (%)	AV (μm^3)	AS (μm^2)	AS–AV (μm^{-1})
FA10JS155	10.2	6.5	386,193	16,747	0.043
FA10JS154	8.3	5	97,002	9,228	0.095
FA10JS149	5.7	5.3	50,359	4,158	0.083
FA10JS150	4.7	4	59,190	7,106	0.120
FA10JS047	2.4	6.2	925,535	32,844	0.035
EC10HC030	8.7	5.7	463,443	23,863	0.051

Note: NMR Ø: NMR porosity; XCT Ø: XCT porosity; AV: average pore volume; AS = average surface area; AS–AV: average surface area over average pore volume.

5 | DISCUSSION

5.1 | NMR-MICP-based reservoir potential of continental spring carbonates and comparison with marine carbonates

The reservoir properties of the continental spring carbonates are heterogeneous, with centimetre to nanometre scaled pores. No distinct porosity and permeability anisotropy was observed for plug samples, except for the sub-horizontal facies with a dominantly pseudo-fenestral pore network. Pore types, such as intramicrite, phyto-mouldic pores (reflecting in life or eroded position), vugs, cement-reduced interparticle pores and framework pores, have the potential to provide well-connected networks in both horizontal and vertical directions. The large macropores in the continental spring carbonates are very often related to phyto-mouldic porosity, which is absent in marine carbonates. The abundance of these large pores is advantageous from a reservoir point of view. At the same time, the entire spectrum of micropores to macropores is covered, generating complex reservoir rocks. Micropores in the continental spring carbonates are found in dendritic features, which are possibly mediated by microorganisms (Claes et al., 2015, 2017b). The petrophysical complexity of continental spring carbonates with large pore types and size ranges is also evidenced by their porosity and permeability heterogeneity. Nurmi (1986) defined porosity and permeability relationships for various marine carbonate rocks, including wackestones, mudstones, chalk, dolomite and grainstones. The defined petrophysical relationships reported by the latter author, however, are not applicable to the studied continental spring carbonates, which yield porosities and permeabilities that span the ranges of all the other carbonate rock types. The high heterogeneity and complexity

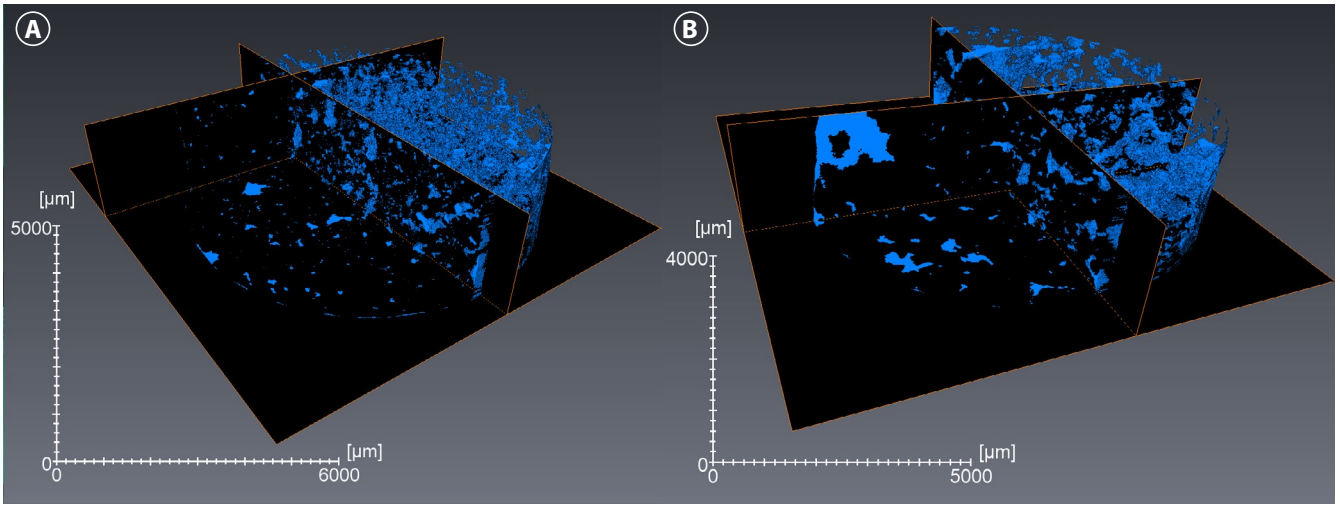

FIGURE 14 Orthogonal slices and partially volume rendered pore networks. (A) Sample FA10JS150 with small pores in a pore distribution with typically 800 < *T*2 < 2,600 ms. (B) Sample FA10JS047 with fewer, but large pores, typical for calculated *T*2 values reaching up to 3,000 ms

of the studied continental spring carbonate samples indicates the need for a coupled investigation with NMR, MICP, XCT and petrography.

A more in depth comparison between the studied continental spring carbonates and marine carbonates is possible based on the MICP and NMR distributions. The latter are given for marine carbonates in Nurmi and Standen (1997), Vincent et al. (2011), Brigaud et al. (2014) and Faÿ-Gomord et al. (2016). Vincent et al. (2011) defined a T_2 cut-off for microporosity in marine carbonates at 200 ms, which proved also to be applicable in continental spring carbonates. The marine types and origin of porosity, however, strongly differ. Marine mudstone and wackestone samples are generally characterised by micropores, often lacking or containing limited amounts of macropores. Their NMR distribution will typically contain short T_2 relaxation times (<200 ms) and Brigaud et al. (2014) reported T_2 modes for microporous carbonates of 55 ms. The distributions obtained in this study have most in common with marine multimodal samples rich in macropores. Marine grainstone samples can yield similar MICP (pore throat radii up to 200 µm) and NMR ranges as the continental spring carbonates, with T_2 modes well over 500 ms (Brigaud et al., 2014). In the marine carbonates with multimodal PSD curves, the macropores are often interparticle, bioclast mouldic and vuggy porosity, while intraparticle porosity or a micritic, muddy matrix is associated with microporosity (Brigaud et al., 2014; Faÿ-Gomord et al., 2016; Nurmi & Standen, 1997; Vincent et al., 2011). The extensive presence of macropores in marine carbonates can furthermore result from processes such as leaching, karstification and brecciation, creating vuggy, mouldic or solution-enlarged mouldic porosity, as for example reported by Léonide et al. (2014) and Cantrell et al. (2020), but these pore types were rarely incorporated in NMR measurements. Even in these macroporous marine carbonates, NMR can be a powerful tool. Ausbrooks et al. (1999) found that MICP distributions correlate with NMR in vuggy carbonates, and that they can be compared with image analysis PSDs. Ouzzane et al. (2006) also highlighted the benefits of NMR in macroporous marine carbonates, as borehole NMR proved sometimes more representative of actual reservoir properties in vuggy carbonates than those obtained from SCAL measurements on core plugs of limited dimensions.

5.2 | NMR porosity and the relationship between pore body and pore throat size

Both NMR and Archimedes porosity have the ability to measure the same pore size spectrum (Anferova et al., 2007) for limestone, sandstone, shale and basalt samples. The NMR porosity depends, however, on the quality of the water saturation. Continental spring carbonate samples contain centimetre-sized macropores. Water loss from these large vugs and moulds, at the exterior of the sample, will result in a lowering of NMR porosity when compared to gas porosity measurements. The deviation from the 1:1 ratio between Archimedes and NMR porosity increases at higher porosity, which potentially indicates that at higher porosity more water loss from the saturated sample occurred.

The observed mismatch between pore throat (MICP) and body (NMR) sizes relates to the difference in measured properties in MICP and NMR respectively. While MICP sees only the connecting pore network and produces the amount of pore space behind a pore throat with a given size, NMR relaxometry sees both patchy distributed macropores and the connecting network, as it depends on the volume to surface ratio of a pore, which relates to the pore body size and shape. Moulds and vugs, for example, which frequently occur in these continental

spring carbonates, will be associated with long relaxation times in NMR, while their connectivity depends on matrix microporosity and mesoporosity and will thus be associated with smaller pore throat sizes. This explains why the $T_{2(lm)}$ overestimates the average pore throat radii size in the samples.

5.3 | NMR distribution types and their connectivity

Mohnke and Klitzsch (2010) described how surface relaxivities depend on mineralogy and hyperfine interactions of fluid nuclei with paramagnetic centers. According to the latter authors, field gradients and changes in magnetic susceptibility will have a bigger impact on smaller pores and will therefore cause varying surface relaxivities for small and large pores. Furthermore, they state that the diffusion regime ($\kappa = \rho r/D$, with ρ the surface relaxation, r the tube radius and D the self-diffusion) influences the NMR PSDs. For intermediate ($1 \ll \kappa \ll 10$) and slow diffusion regimes ($\kappa \gg 10$), in the presence of magnetic field gradients, the relaxation behaviour will become diffusion limited and the system will become characterised by an ensemble of relaxation times. The diffusion regime of the XCT scanned samples in this study was estimated according to the theory described in Müller-Petke et al. (2015). Table 5 lists the diffusion regime (κ) statistics. The samples were all characterised by median and average values for $\kappa \ll 1$, and fast diffusion regimes were thus expected. Some of the largest pores, however, resulted in an intermediate diffusion regime. The limited amount of pores with $1 \ll \kappa \ll 10$ (only 1 pore in EC10HC030, up to only 7 in FA10JS149) could therefore have been accompanied by multi-exponential NMR signals, which could have induced additional short relaxation signals. The samples studied here, however, were almost entirely composed of calcite (Khatib et al., 2014; Özkul et al., 2013; Soete et al., 2015) and pore size related variations in surface relaxivity are therefore expected to be limited. Magnetic field gradients are likely absent in this calcite system and ensure surface limited relaxation behaviour even in intermediate diffusion regimes.

Unimodal, bimodal and atypical PSD types were observed for the continental spring carbonate samples (Figure 8). The sub-horizontal and cascade facies, where peloidal lithotypes dominate, produce dominantly unimodal distributions. Their pore network consists of mesopores and macropores, which together generate flow paths through the sample. In unimodal samples (Figure 15A), the macropores are partly isolated by cements, but are regularly communicating with the mesoporous matrix (Figure 15B). The biostromal reed and waterfall facies, where phyto-lithotypes dominate, produce almost exclusively bimodal or atypical distributions, given in Figure 15C. The presence of micropores in the dendrites surrounding phyto-moulds explains the extension of NMR T_2 distributions for bimodal and atypical samples towards relaxation times below the microporosity cut-off. Pore coupling, frequently encountered in carbonates (Anand & Hirasaki, 2007; Fleury & Soualem, 2009; Moss, 2000; Vincent et al., 2011) explains why NMR curves for bimodal and atypical samples have distinct distributions. The presence or absence of isolating cement rims, in atypical and bimodal samples respectively, determines if the pore network appears coupled or decoupled. In the atypical samples, with bimodal MICP, but unimodal NMR distributions, a coupled pore system occurs due to diffusion and mixing between the microporous compartment on the one hand, and the mesoporous and macroporous compartment on the other (Vincent et al., 2011). Atypical samples are characterised by the same rock fabrics as bimodal samples, but are barely affected by cementation, or show signs of alterations of the cement rims, by for example dissolution or fracturing (Figure 10J). Long dendrites, for which plants acted as a nucleation site, are at many places in direct contact with reed mouldic pores. The micropores in the dendrites can in this case communicate with mesopores and macropores and coupled pore systems with unimodal NMR distributions will be the result (Figure 10K).

When dendrites are encapsulated in an envelope of sparites (Figure 10G,H), water molecules exploring the rock surface are unable to travel from the micropore compartment (Figure 15D), i.e., from within the dendrites, to the mesopore and macropore compartments. A bimodal NMR T_2 distribution

TABLE 5 Diffusion regime ($\kappa = \rho r—D$) statistics

Sample	FA10JS155	FA10JS154	FA10JS150	FA10JS149	FA10JS047	EC10HC030
Minimum	0.005	0.003	0.003	0.003	0.003	0.003
Maximum	2.307	4.548	2.923	1.428	1.647	5.341
Average	0.024	0.021	0.021	0.014	0.037	0.029
Median	0.014	0.013	0.012	0.008	0.021	0.017
Standard deviation	0.052	0.037	0.031	0.025	0.071	0.064
# pores	15,216	47,775	60,995	89,154	6,000	11,521
# pores with $\rho r—D \geq 1$	5	6	3	7	6	1

Note: Diffusion regime (κ) calculated as a function of the surface relaxation (ρ), tube radius (r) and self-diffusion (D).

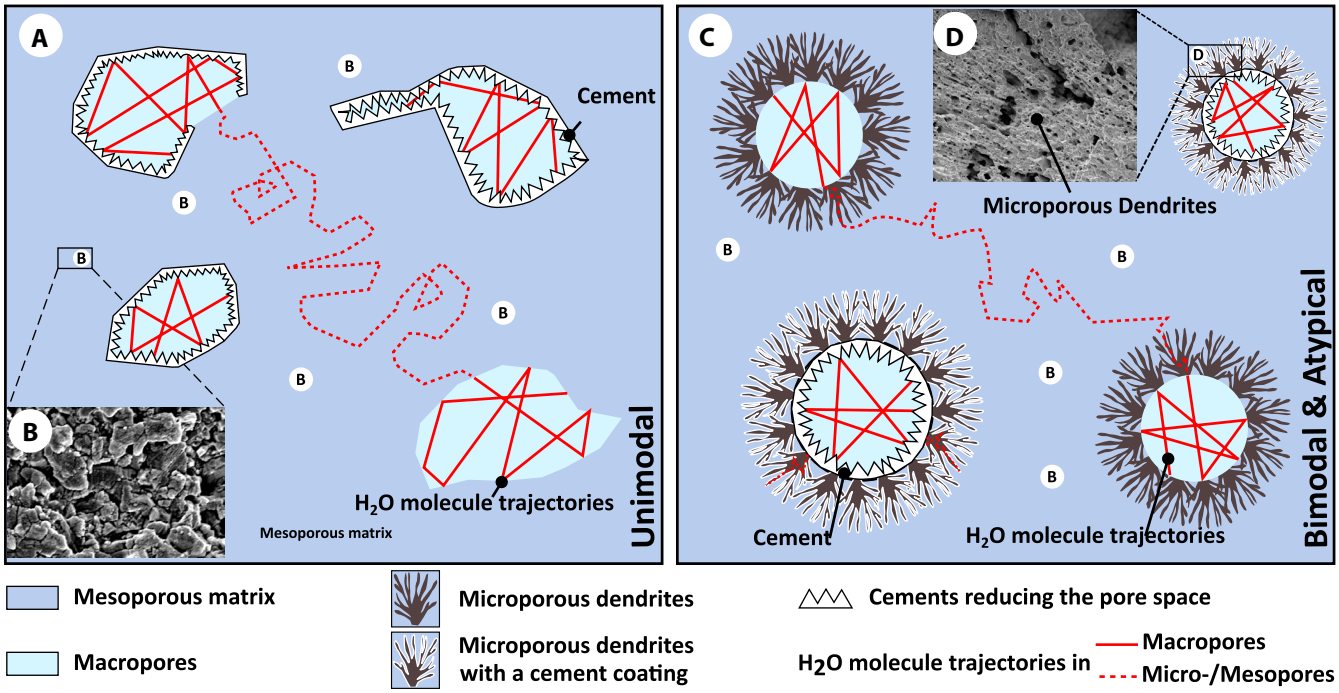

FIGURE 15 Conceptual models of the envisioned fluid flow trajectories. (A) Unimodal samples with macropores that are partly reduced by cements, but regularly communicate with the mesoporous matrix. (B) Detailed SEM image of the mesoporous matrix. (C) Uncemented atypical samples and cement reduced bimodal samples, where a sparite rim isolates microporous dendrites, from the meso- and macropore compartment. In the case of atypical samples, all pore compartments are connected and lead to pore coupling during NMR analysis. (D) SEM image of microporous dendrites

will in this case develop (Figure 10I). Bimodal samples are typically highly porous, but with limited permeability. Petrography (SEM, PLM and FM) showed that isopachous, non-porous sparite rims, encapsulating dendritic structures, isolate micropores from the rest of the pore system. The cementation not only decouples pore compartments, but overall limits the connectivity (<10 mD) between macropores. One bimodal sample (Figure 9A) yields a lower porosity (9%) and higher permeability (178 mD) than expected. This sample is dominated by the phyto-lithotype, just like the other bimodal samples, but the phyto-lithotype sub-category is different. The sample is dominated by the smaller grass phyto-lithotype (smaller plants types, pore diameters <2 mm; Claes et al., 2015). The grass casts are reduced by cement, but still present an open pore structure, in which all grass moulds follow the same orientation (growth position). The alignment of the smaller, but far more abundant and more uniformly distributed pores explains the difference in petrophysical characteristics for this bimodal outlier.

The MICP-NMR distributions play a crucial role in recognising characteristic pore network properties within carbonate bodies. Nevertheless, given the pore network heterogeneity in continental spring carbonates, predicting permeability remains complicated. A quantitative prediction could be achieved by considering electrical conductivity measurements (scope of future research projects). The obtained information about pore connectivity and tortuosity would be helpful in understanding the permeability of the continental spring carbonates, e.g., as suggested by Katz and Thompson (1986). The described microporosity T_2 cut-off relates to pore size and was defined based on the comparison of MICP and NMR distributions. The SDR model was applied to calculate permeability based on the obtained $T_{2(lm)}$ data, but the model did not provide good permeability predictions. As an alternative, Belila et al. (2020) demonstrated that performing irreducible water saturation experiments is useful to define the Free-Fluid Index (FFI) and the bulk volume irreducible (BVI) and consequently a FFI/BVI T_2 cut-off of the pore network. This T_2 cut-off can in turn be used to calculate permeability using the Timur–Coates equations. Katz and Thompson (1986) stated the need to use different FFI/BVI cut-offs for different petrophysical sample groups in strongly heterogeneous pore networks. In line with these findings, it is expected that unimodal, bimodal and atypical samples will yield different FFI/BVI T_2 cut-offs, with the lowest cut-off expected for atypical samples, where the compartments are coupled and hence the free fluid index is expected to be higher. Sparite cementation causes decoupling of the pore compartments, as for example in bimodal samples, and will therefore likely result in a larger BVI. Adapted FFI/BVI T_2 cut-offs for different petrophysical sample types are expected to strongly improve NMR based permeability estimations. Boyd et al. (2015) analysed the NMR response of oil-wet carbonates

in Presalt core samples, oil samples and oil-based mud filtrate at downhole conditions. The authors showed that laboratory measurements are crucial in understanding how varying wettability and surface relaxivity affect the NMR T_2 response. In addition, this study shows that laboratory measurements are valuable in understanding the link between the NMR response, the pore sizes and connectivity between the pore compartments in continental spring carbonates. Both studies put forward that a multidisciplinary approach is required to uncover the pore network properties of these heterogeneous carbonates.

5.4 | Calibration between NMR and XCT

The calculated XCT PSDs are consistent with the NMR distributions at $T_2 > 700$ ms (Figure 13). The absence of T_2 estimates <700 ms indicates that micropores are completely absent and that mesopores are partially missing in the XCT scan data. The shape of the XCT calculated PSDs relates to sample porosity and pore size. The pore size occurrence frequency dictates the amplitudes of the XCT PSD, while pore size itself is used to calculate T_2. With increasing pore size, the pore volume increases significantly faster than the pore area. Consequently, larger pores are typically characterised by lower S/V ratios and will, in accordance with Equation 11, result in longer XCT deduced T_2-times. Slight differences in the ranges for the XCT T_2 values can be observed for two samples in Figure 13A,B. Assumptions had to be made to calculate the XCT T_2 distribution. The pore shape, for example, was assumed ellipsoidal, which is a simplification of the real pore structure. Furthermore, the XCT T_2 distributions were corrected for bulk relaxivity in a less sophisticated way, namely by simply subtracting T_{2b}. The simplifications could slightly affect the calculated T_2 ranges, but overall observations are expected to be valid.

In XCT studies there is a trade-off between resolution and sample size. Since the aim here was to compare NMR PSD curves with XCT data, the focus was on obtaining the best possible spatial resolution and hence resolving pore objects as small as possible. Therefore, mini-plugs that do not necessarily reach the size of the representative elementary volume, were scanned with XCT, allowing high resolution 3D datasets to be obtained. The observed discrepancies between NMR and XCT porosity could thus relate to the difference in analysed sample volume. A XCT mini-plug, taken from more porous parts of a larger NMR plug, might for example explain the higher XCT porosities when compared to the NMR porosity for sample FA10JS047 (Table 4). An alternative explanation for the higher XCT porosity is incomplete saturation of this sample prior to the NMR measurements, which would result in lowered NMR porosity. Despite the difference in sample size for XCT and NMR, a general trend with lower calculated XCT porosities is observed, and is most likely indicative of the unrecorded fraction of micropores and mesopores in XCT scans. The microporous and mesoporous areas, observed in XCT as zones with tomodensities that fall between rock and pore ranges (Figure 10F), indicate that the generally lower XCT porosity can at least partially be attributed to the presence of micropores and mesopores that were not, or not fully, resolved in XCT reconstructed datasets.

The XCT complements MICP and NMR by providing digital pore network data with pore sizes up to several centimetres, i.e., much larger than what can be measured with MICP or laboratory NMR. Volume renderings can facilitate the 3D understanding of the porous network in reservoir rocks, especially since even structures at the lower margin of the resolution can be interpreted by comparison with petrography, MICP and NMR data. The XCT based calculations of reservoir properties should, however, be interpreted with caution. Low tomodensity areas in the XCT images were recognised as microporous and mesoporous structures, but the individual pore bodies were not sufficiently resolved to be labelled or quantitatively analysed. The MICP-NMR analysis showed that micropores and mesopores are of importance for reservoir properties in continental spring carbonates, which means that excluding these pores will lead to incorrect predictions of porosity and permeability. This study demonstrates in accordance with observations made by Soete et al. (2017) that, while building rock models, covering multiple spatial scales (micron to macroscale) it is necessary to generate valid digital models and to perform representative digital rock petrophysics. Multi-scale imaging and data integration from micron to macrometre-scale, with for example Multiple-Point geoStatistics (MPS), are required to achieve that goal with present day techniques and/or generative adversarial neural networks (Caers & Zhang, 2004; Janssens et al., 2020; Journel & Zhang, 2006; Okabe & Blunt, 2004).

6 | CONCLUSION

Four different continental spring carbonate facies, i.e., the sub-horizontal, biostromal reed, cascade and waterfall facies, are well exposed in the Ballık area (Turkey). Petrography allowed identification of different pore types: intramicrite, intracrystalline, intercrystalline, cement-reduced interparticle, vuggy and mouldic porosity. These pore types produce complex pore networks with large pore size variability. The heterogeneous continental spring carbonates, exhibit large-scale ranges for both porosity (3%–25%) and permeability (0.004–3,675 mD). The facies classification is insufficient to link porosity and permeability, due to intrafacies pore network variability. Better assessment of reservoir properties can be achieved by subdividing facies into lithotype and pore type classes.

The continental spring carbonate samples were subdivided into three categories based on MICP pore throat radii (r) and NMR T_2 distributions. (a) Unimodal samples, with one pore compartment containing macropores (r = 15–200 μm) and mesopores (r = 1–15 μm); (b) Bimodal samples; and (c) Atypical samples with an additional microporous compartment (r < 1 μm). The sample category is lithotype dependent. Unimodal samples are dominated by the peloidal lithotype, which dominates the sub-horizontal and cascade facies. Macropores in the distribution originate from intercrystal, vuggy, mouldic and cement-reduced interparticle porosity. Mesoporosity comprises intramicrite and intracrystalline porosity. Bimodal and atypical samples are dominated by phyto-lithotypes, which mainly occur in the biostromal reed and waterfall facies. Micropores are found inside micritic dendritic structures, which overgrow plants and are as a consequence found around mouldic pores. The microporous dendrites extend the NMR distributions for bimodal and atypical samples towards relaxation times below the microporosity cut-off value (T_2 < 200 ms). The atypical sample types contain NMR and MICP distributions that are not in good correspondence, since they are affected by diffusional pore coupling. Decoupling is observed in the presence of isopachous, non-porous sparite rims coating the dendrites, which isolate the micropores.

This study demonstrates that there is a link between porosity, permeability and the type of MICP-NMR distribution and thus indirectly with the lithotypes and pore types. Phyto-dominated bimodal samples are typically highly porous (mainly 15%–25%), but their permeability is generally lower (mainly < 5 mD) when compared to atypical and unimodal samples. The cements reduce pores, decreasing the permeability. The decoupled dendritic micropore compartments increase the porosity, but do not significantly contribute to the permeability. Peloidal dominated unimodal samples have porosities < 16% and permeabilities below 1,000 mD. The highest permeabilities are encountered in phyto-dominated atypical samples, with coupled compartments (>3,500 mD). With NMR core logging, an upscaling from the plug measurements performed here to core scale observations can be achieved. The resulting PSDs could play a crucial role in recognising units with characteristic pore network properties within continental spring carbonate bodies.

Petrography, MICP, NMR and XCT complement each other by providing (a) a rock and pore typing through thin section petrography and SEM imaging, (b) pore throat sizes (MICP), (c) information on *V/S* pore ratios, as a proxy for pore size (NMR), (d) information on pore compartment connectivity (MICP and NMR) and (e) 3D digital pore network data (CT). Together these techniques allow detailed pore network characterisation, as they cover multiple spatial scales (microscale to macroscale). The 3D XCT renderings facilitate the understanding of the porous network in reservoir rocks, but caution is advised when performing digital rock petrophysics. Micropores and a portion of mesopores, which proved to play a vital role in the pore connectivity, likely fall below the resolution of current industrial XCT scanners. The multidisciplinary approach applied here combines the advantages of the standalone methods and therefore overcomes many of their shortcomings.

ACKNOWLEDGEMENTS

Our thanks go to the owners and managers of Faber and Ece, for providing us with the opportunity to work in their active quarries. We would like to thank Herman Nijs, for the preparation of the thin sections and his assistance with practical matters during the sample preparation processes. The authors would like to acknowledge the Hercules Foundation (Flanders) for founding the micro- and nano-XCT project for the hierarchical analysis of materials. We are grateful to Rudy De Vos for assisting in the E-SEM petrography and Evy Vereecken for her help and guidance during the MICP measurements and the interpretation of the data. Soete J. was a PhD grant holder from 'Agentschap voor Innovatie door Wetenschap en Technologie' (IWT), Flanders, Belgium.

CONFLICT OF INTEREST

The authors declare that there is no conflict of interest regarding the publication of this paper.

ORCID

Jeroen Soete https://orcid.org/0000-0003-3357-4070
Hannes Claes https://orcid.org/0000-0002-2424-6975

REFERENCES

Alabi, G., Kasten, R., Chitale, V., Yadavalli, S. & Piccoli, L. (2014) The value of petrophysical measurements across multiple scales. A lacustrine carbonate example from Campos Basin, Brazil. *SPWLA 55th annual logging symposium*, May 18–22.

Alçiçek, H., Varol, B. & Özkul, M. (2007) Sedimentary facies, depositional environments and palaeogeographic evolution of the Neogene Denizli Basin, SW Anatolia, Turkey. *Sedimentary Geology*, *202*(4), 596–637.

Anand, V. & Hirasaki, G.J. (2007) Diffusional coupling between micro and macroporosity for NMR relaxation in sandstones and grainstones. *Petrophysics*, *48*(4), 289–307.

Anferova, S., Anferov, V., Arnold, J., Talnishnikh, E., Voda, M.A., Kupferschläger, K. et al. (2007) Improved Halbach sensor for NMR scanning of drill cores. *Magnetic Resonance Imaging*, *25*(4), 474–480.

Aratman, C., Özkul, M., Swennen, R., Hollis, C., Erthal, M.M., Claes, H. et al. (2020) The giant Quaternary Ballik travertine system in the Denizli Basin (SW Turkey): A peleoenvironmental analysis. *Quaternaire*, *30*(2), 91–116.

Ausbrooks, N.S., Hurley, N.F., May, A. & Neese, D.G. (1999) Pore-size distributions in vuggy carbonates from core images, NMR, and capillary pressure. SPE Annual Technical Conference and Exhibition, 3–6 October, Houston, Texas Publication Date 1999, SPE-56506-MS.

Belila, A.M.P., Basso, M., Chinelatto, G.F., Kuroda, M.C., Vidal, A.C. (2020) Pore typing using nuclear magnetic resonance, an example with samples from cretaceous Pre-Salt lacustrine carbonates in the Santos Basin, Brazil. *Journal of Petroleum Science and Engineering*, *190*, 107079.

Boyd, A., Souza, A., Carneiro, G., Machado, V., Trevizan, W., Santos, B. et al. (2015) Presalt carbonate evaluation for Santos basin, Offshore Brazil. *Petrophysics*, *56*(6), 577–591.

Bozkurt, C. & Bozkurt, E. (2009) Pattern of normal faulting in the Gediz Graben, SW Turkey. *Tectonophysics*, *473*(1–2), 234–260.

Brigaud, B., Vincent, B., Durlet, C., Deconinck, J.F., Jobard, E., Pickard, N. et al. (2014) Characterization and origin of permeability-porosity heterogeneity in shallow-marine carbonates: From core scale to 3D reservoir dimension (Middle Jurassic, Paris Basin, France). *Marine and Petroleum Geology*, *57*, 631–651.

Caers, J. & Zhang, T. (2004) Multiple-point geostatistics: A quantitative vehicle for integrating geologic analogs into multiple reservoir models. In: Grammer, G.M., Harris, P.M. & Eberli, G.P. (Eds.) *Integration of outcrop and modern analogs in reservoir modelling*. *AAPG Memoir 80*, 383–394.

Cantrell, D.L., Shah, R.A., Ou, J., Xu, C., Phillips, C., Li, X.L. et al. (2020) Depositional and diagenetic controls on reservoir quality: Example from the upper Cretaceous Mishrif Formation of Iraq. *Marine and Petroleum Geology*, *118*, 104415.

Chitale, V., Alabi, G., Kasten, R., Taylor, A. & Hoenmans, P. (2014) Learning from deployment of a variety of modern petrophysical formation evaluation technologies and techniques for characterization of a Pre-Salt carbonate reservoir: Case study from Campos Basin, Brazil. *SPWLA 55th annual logging symposium*, May 18–22.

Claes, H., Degros, M., Soete, J., Claes, S., Kele, S., Mindszenty, A. et al. (2017a) Geobody architecture, genesis and petrophysical characteristics of the Budakalász travertines, Buda Hills (Hungary). *Quaternary International*, *437*, 107–128.

Claes, H., Erthal, M.M., Soete, J., Özkul, M. & Swennen, R. (2017b) Shrub and pore type classification: Petrography of travertine shrubs from the Ballik-Belevi area (Denizli, SW Turkey). *Quaternary International*, *437*, 147–163.

Claes, H., Huysmans, M., Soete, J., Dirix, K., Vassilieva, E., Erthal, M.M., et al. (2019) Elemental geochemistry to complement stable isotope data of fossil travertine: Importance of digestion method and statistics. *Sedimentary Geology*, *386*, 118–131. https://doi.org/10.1016/j.sedgeo.2019.04.002.

Claes, H., Soete, J., Van Noten, K., El Desouky, H., Marques Erthal, M., Vanhaecke, F. et al. (2015) Sedimentology, three-dimensional geobody reconstruction and carbon dioxide origin of Pleistocene travertine deposits in the Ballık area (south-west Turkey). *Sedimentology*, *62*, 1408–1445.

Claes, H., Török, A., Soete, J., Mohammadi, Z., Vassilieva, E., Hamaekers, H. et al. (2020) U/TH dating and open system behavior: implications for travertines based on the study of Süttő (Hungary) and Ballik (Turkey) sites. *Quaternaire*, *30*(2), 117–132.

Claes, S., Soete, J., Cnudde, V. & Swennen, R. (2016) A 3D classification for mathematical pore shape description in complex carbonate reservoir rocks. *Mathematical Geosciences*, *48*(6), 619–639.

Coates, G.R., Xiao, L. & Prammer, M.G. (2001) *NMR logging: Principles and applications*. Houston, TX: Halliburton Energy Services, 234 pp. Printed in the United States of America (Houston)

Crain, E.R. (2019) *Crain's petrophysical handbook*. Spectrum, 193 pp. http://www.spec2000.net. [Accessed April, 2011].

De Boever, E., Foubert, A., Lopez, B., Swennen, R., Jaworowski, C., Özkul, M. et al. (2017) Comparative study of the Pleistocene Cakmak quarry (Denizli Basin, Turkey) and modern Mammoth Hot Springs deposits (Yellowstone National Park, USA). *Quaternary International*, *437*, 129–146.

De Boever, E., Foubert, A., Oligschlaeger, D., Claes, S., Soete, J., Bertier, P. et al. (2016) Multiscale approach to (micro)porosity quantification in continental spring carbonate facies: Case study from the Cakmak quarry (Denizli, Turkey). *American Geophysical Union*, *17*(7), 2922–2939.

De Fillippis, L., Faccenna, C., Billi, A., Anzalone, E., Brilli, M., Özkul, M. et al. (2012) Growth of fissure ridge travertines from geothermal springs of Denizli Basin, western Turkey. *Geological Society of America Bulletin*, *124*(9), 1629–1645.

Della Porta, G., Croci, A., Marini, M. & Kele, S. (2017) Depositional architecture, facies character and geochemical signature of the Tivoli travertines (pleistocene, acque albule basin, central Italy). *Rivista Italiana di Paleontologia e Stratigrafia*, *123*(3), 487–540.

Deville de Periere, M., Durlet, C., Vennin, E., Lambert, L., Bourillot, R., Caline, B. et al. (2011) Morphometry of micrite particles in Cretaceous microporous limestones of the Middle East: Influence on reservoir properties. *Marine and Petroleum Geology*, *28*(9), 1727–1750.

Dewit, J., Huysmans, M., Muchez, P., Hunt, D.W., Thurmond, J.B., Verges, J. et al. (2012) Reservoir characteristics of fault-controlled hydrothermal dolomite bodies: Ramales Platform case study. *Geological Society, London, Special Publications*, *370*(1), 83–109.

Diniz-Ferreira, E.L. & Torres-Verdín, C. (2012) Improved estimation of pore connectivity and permeability in deepwater carbonates with the construction of multi-layer static and dynamic petrophysical models. *SPWLA 53rd Annual Logging Symposium*, 16–20 June.

Eberli, G.P., Baechle, G.T., Anselmetti, F.S. & Incze, M.L. (2003) Factors controlling elastic properties in carbonate sediments and rocks. *The Leading Edge*, *22*, 654–660.

Ehrenberg, S.N., Eberli, G.P. & Baechle, G. (2006) Porosity – Permeability relationships in Miocene carbonate platforms and slopes seaward of the Great Barrier Reef, Australia (ODP Leg 194, Marion Plateau). *Sedimentology*, *53*(6), 1289–1318.

El Desouky, H., Soete, J., Claes, H., Özkul, M., Vanhaecke, F. & Swennen, R. (2015) Novel applications of fluid inclusions and isotope geochemistry in unravelling the genesis of fossil travertine systems. *Sedimentology*, *62*(1), 27–56.

Erdoğan, O. & Özvan, A. (2015) Evaluation of strength parameters and quality assessment of different lithotype levels of Edremit (Van) Travertine (Eastern Turkey). *Journal of African Earth Sciences*, *106*, 108–117.

Erthal, M.M., Capezzuoli, E., Mancini, A., Claes, H., Soete, J. & Swennen, R. (2017) Shrub morpho-types as indicator for the water flow energy – Tivoli travertine case (Central Italy). *Sedimentary Geology*, *347*, 79–99.

Faÿ-Gomord, O., Soete, J., Katika, K., Galaup, S., Caline, B., Descamps, F. et al. (2016) New insight into the microtexture of chalks from NMR analysis. *Marine and Petroleum Geology*, *75*, 252–271.

Fleury, M., Deflandre, F. & Godefroy, S. (2001) Validity of permeability prediction from NMR measurements. *Comptes Rendus de l'Academie des Sciences – Series IIc: Chemistry*, *4*, 869–872.

Fleury, M. & Soualem, J. (2009) Quantitative analysis of diffusional pore coupling from T2-store-T2 NMR experiments. *Journal of Colloid and Interface Science*, *336*(1), 250–259.

Ford, T.D. & Pedley, H.M. (1996) A review of tufa and travertine deposits of the world. *Earth-Science Reviews*, *41*(3–4), 117–175.

Giesche, H. (2006) Mercury porosimetry: A general (practical) overview. *Particle & Particle Systems Characterization*, *23*(1), 9–19.

Grunewald, E. & Knight, R. (2009) A laboratory study of NMR relaxation times and pore coupling in heterogeneous media. *Geophysics*, *74*(6), E215–E221.

Guo, L. & Riding, R. (1998) Hot-spring travertine facies and sequences, Late Pleistocene, Rapolano Terme, Italy. *Sedimentology*, *45*(1), 163–180.

Gürbüz, A., Boyraz, S. & Ismael, M.T. (2012) Plio-Quaternary development of the Baklan-Dinar graben: Implications for cross-graben formation in SW Turkey. *International Geology Review*, *54*(1), 33–50.

Gürer, Ö.F. & Yilmaz, Y. (2002) Geology of the Ören and surrounding areas, SW Anatolia. *Turkish Journal of Earth Sciences*, *11*, 1–13.

Hancock, P.L., Chalmers, R.M.L., Altunel, E., ÇAkir, Z., and Becher-Hancock, A. (2000) Creation and destruction of travertine monumental stone by earthquake faulting at Hierapolis, Turkey. *Geological Society, London, Special Publications*, *171*(1), 1–14.

Janssens, N., Huysmans, M. & Swennen, R. (2020) Computed tomography 3D super-resolution with generative adversarial neural networks: Implications on unsaturated and two-phase fluid flow. *Materials (Basel)*, *13*(6), 1–33.

Journel, A. & Zhang, T. (2006) The necessity of a multiple-point prior model. *Mathematical Geology*, *38*(5), 591–610.

Kaczmarek, S.E., Fullmer, S.M. & Hasiuk, F.J. (2015) A universal classification scheme for the microcrystals that host limestone microporosity. *Journal of Sedimentary Research*, *85*(10), 1197–1212.

Katz, A.J. & Thompson, A.H. (1986) Quantitative prediction of permeability and electrical conductivity in porous rock. *The American Physical Society*, *34*(11), 6–7.

Kaymakci, N. (2006) Kinematic development and paleostress analysis of the Denizli Basin (Western Turkey): Implications of spatial variation of relative paleostress magnitudes and orientations. *Journal of Asian Earth Sciences*, *27*(2), 207–222.

Kele, S., Özkul, M., Fórizs, I., Gökgöz, A., Baykara, M.O., Alçiçek, M.C. et al. (2011) Stable isotope geochemical study of Pamukkale travertines: New evidences of low-temperature non-equilibrium calcite-water fractionation. *Sedimentary Geology*, *238*(1–2), 191–212.

Kenyon, W.E. (1997) Petrophysical principles of applications of NMR logging. *The Log Analyst*, *38*(2), 21–43.

Khatib, S., Rochette, P., Alçiçek, M.C., Lebatard, A.-E., Demory, F. & Saos, T. (2014) Études stratigraphique, sédimentologique et paléomagnétique des travertins de Kocabaş, Bassin de Denizli, Anatolie, Turquie, contenant des restes fossiles quaternaires. *L'Anthropologie*, *118*(1), 16–33.

Koçyiğit, A. & Deveci, Ş. (2007) A N – S-trending active extensional structure, the Şuhut (Afyon) Graben: Commencement age of the extensional Neotectonic period in the Isparta Angle, SW Turkey. *Turkish Journal of Earth Sciences*, *16*, 391–416.

Lapponi, F., Casini, G., Sharp, I., Blendinger, W., Fernandez, N., Romaire, I. et al. (2011) From outcrop to 3D modelling: A case study of a dolomitized carbonate reservoir, Zagros Mountains, Iran. *Petroleum Geoscience*, *17*(3), 283–307.

Lebatard, A.-E., Alçiçek, M.C., Rochette, P., Khatib, S., Vialet, A., Boulbes, N. et al. (2014) Dating the Homo erectus bearing travertine from Kocabaş (Denizli, Turkey) at at least 1.1 Ma. *Earth and Planetary Science Letters*, *390*, 8–18.

Lenormand, R. (2003) Interpretation of mercury injection curves to derive pore size distribution. *International symposium of the society of core analysts*. pp. SCA2003-52.

Léonide, P., Fournier, F., Reijmer, J.J.G., Vonhof, H., Borgomano, J., Dijk, J. et al. (2014) Diagenetic patterns and pore space distribution along a platform to outer-shelf transect (Urgonian limestone, Barremian-Aptian, SE France). *Sedimentary Geology*, *306*, 1–23.

Lopez, B., Camoin, G., Özkul, M., Swennen, R. & Virgone, A. (2017) Sedimentology of coexisting travertine and tufa deposits in a mounded geothermal spring carbonate system, Obruktepe, Turkey. *Sedimentology*, *64*(4), 903–931.

Lucia, F.J. (2007) *Carbonate reservoir characterization*, 2nd edition. New York: Springer.

Mancini, E.A., Morgan, W.A., Harris, P.M. & Parcell, W.C. 2013. Introduction: AAPG Hedberg Research Conference on microbial carbonate reservoir characterization—Conference summary and selected papers. *AAPG Bulletin*, *97*(11), 1835–1847.

Mavko, G., Mukerji, T. & Dvorkin, J. (2009) *The rock physics handbook*, 2nd edition. Cambridge: Cambridge University Press.

Melim, L.A., Anselmetti, F.S. & Eberli, G.P. (2001) The importance of pore type on permeability of Neogene carbonates, Great Bahama Bank. In: Ginsburg, R.N. (Ed.), *Subsurface geology of a prograding carbonate platform margin, great Bahama Bank: Results of the Bahamas Drilling Project*. *SEPM Spec Publ*, *70*, 217–240.

Minh, C.C., Petricola, M. & Dennis, B. (1997) The carbonate challenge. *Middle East Well Evaluation Review*, *20*(19), 33–55.

Mohammadi, Z., Claes, H., Capezzuoli, E., Mozafari, M., Soete, J., Aratman, C. et al. (2020) Lateral and vertical variations in sedimentology and geochemistry of sub-horizontal laminated travertines (Çakmak quarry, Denizli Basin, Turkey). *Quaternary International*, *540*, 146–168.

Mohnke, O. (2014) Jointly deriving NMR surface relaxivity and pore-size distributions by NMR relaxation experiments on partially desaturated rocks. *American Geophysical Union*, *50*(6), 5309–5321.

Mohnke, O. & Klitzsch, N. (2010) Microscale simulations of NMR relaxation in porous media considering internal field gradients. *Vadose Zone Journal*, *9*(4), 846–857.

Moss, A.K. (2000) The ART NMR carbonate rock catalogue: A library of NMR response characteristics in carbonate rocks. *DiaLog*, *8*(3), 1–5.

Müller-Petke, M., Dlugosch, R., Lehmann-Horn, J. & Ronczka, M. (2015) Nuclear magnetic resonance average pore-size estimations outside the fast-diffusion regime. *Geophysics*, *80*(3), D195–D206.

Nurmi, R. (1986) Land of the giants. *Middle East Well Evaluation Review*, *1*, 6–21.

Nurmi, R. & Standen, E. (1997) Carbonates, the inside story. *Middle East Well Evaluation Review*, *18*, 28–41.

Okabe, H. & Blunt, M.J. (2004) Prediction of permeability for porous media reconstructed using multiple-point statistics. *Physical Review E*, *70*(6), 066135.

Ouzzane, J.E., Ramamoorthy, R., Boyd, A.J., Rose, D.A., Okuyiga, M. & Nasser, G. (2006) Application of NMR T2 relaxation for drainage capillary pressure in vuggy carbonate reservoirs. *SPE Annual Technical Conference and Exhibition*, 24–27 September, San Antonio, Texas, USA, SPE-101897-MS.

Özkul, M., Gökgöz, A. & HorvatincIc, N. (2010) Depositional properties and geochemistry of Holocene perched springline tufa deposits and associated spring waters: A case study from the Denizli Province, Western Turkey. *Geological Society, London, Special Publications*, *336*(1), 245–262.

Özkul, M., Kele, S., Gökgöz, A., Shen, C.-C., Jones, B., Baykara, M.O. et al. (2013) Comparison of the Quaternary travertine sites in the

Denizli extensional basin based on their depositional and geochemical data. *Sedimentary Geology*, *294*, 179–204.

Özkul, M., Varol, B. & Alçiçek, M.C. (2002) Depositional environments and petrography of denizli travertines. *Bulletin of the Mineral Research and Exploration*, *125*(125), 13–29.

Pedley, H.M. & Rogerson, M. (2010) *Tufas and speleothems unravelling the microbial and physical controls*. London: Geological Society of London, Special Publication, 684 pp.

Pentecost, A. (2005) *Travertine*. New York: Geologist Association: Springer, 495 pp.

Purcell, W.R. (1949) Capillary pressures – Their measurement using mercury and the calculation of permeability therefrom. *Journal of Petroleum Technology*, *1*(2), 39–48.

Rezaee, M.R., Jafari, A. & Kazemzadeh, E. (2006) Relationships between permeability, porosity and pore throat size in carbonate rocks using regression analysis and neural networks. *Journal of Geophysics and Engineering*, *3*(4), 370–376.

Rezende, M.F. & Pope, M.C. (2015) Importance of depositional texture in pore characterization of subsalt microbialite carbonates, offshore Brazil. *Geological Society, London, Special Publications*, *418*(1), 193–207.

Ronchi, P. & Cruciani, F. (2015) Continental carbonates as a hydrocarbon reservoir, an analogue case study from the Travertine of Saturnia, Italy. *AAPG Bulletin*, *99*(4), 711–734.

Saldaña, M., González, J., Pérez-Rey, I., Jeldres, M. & Toro, N. (2020) Applying statistical analysis and machine learning for modeling the UCS from P-wave velocity, density and porosity on dry travertine. *Applied Sciences*, *10*, 4565–4579.

Saller, A., Rushton, S., Buambua, L., Inman, K., McNeil, R. & Dickson, J.A.D. (2016) Presalt stratigraphy and depositional systems in the Kwanza Basin, offshore Angola. *AAPG Bulletin*, *100*(7), 1135–1164.

Schlumberger Limited (2015) *Oilfield Glossary, microporosity*. Available at: http://www.glossary.oilfield.slb.com/en/Terms/m/microporosity.aspx [Accessed 21st August 2015]

Schröder, S., Ibekwe, A., Saunders, M., Dixon, R. & Fisher, A. (2016) Algal–microbial carbonates of the Namibe Basin (Albian, Angola): Implications for microbial carbonate mound development in the South Atlantic. *Petroleum Geoscience*, *22*, 71–90.

Sharp, I., Verwer, K., Ferreira, H., Lapponi, F., Snidero, M., Machado, V. et al. (2013) Pre- and post-salt non-marine carbonates of the Namibe Basin, Angola. Programme and abstract volume: Microbial carbonates in space and time: Implications for global exploration and production. The Geological Society, London, 19−20 June, pp. 52–53.

Soete, J. (2016) Pore network characterization in complex carbonate systems, a multidisciplinary approach. Thesis presented in pursuit of the degree of Doctor in Sciences, Earth-and environmental sciences, Faculty of Sciences, KU Leuven.

Soete, J., Claes, S., Claes, H., Janssens, N., Cnudde, V., Huysmans, M. & Swennen, R. (2017) Lattice boltzmann simulations of fluid flow in continental carbonate reservoir rocks and in upscaled rock models generated with multiple-point geostatistics. *Geofluids*, *24*, 1–24. https://doi.org/10.1155/2017/7240524

Soete, J., Kleipool, L.M., Claes, H., Claes, S., Hamaekers, H., Kele, S. et al. (2015) Acoustic properties in travertines and their relation to porosity and pore types. *Marine and Petroleum Geology*, *59*, 320–335.

Terra, J.G.S., Spadini, A.R., França, A.B., Leite, C., Zambonato, E.E., Costa, L. et al. (2010) Classificações clássicas de rochas carbonáticas. *Boletim de Geociencias da Petrobras, Rio de Janeiro*, *18*(1), 9–29.

Török, Á., Mindszenty, A., Claes, H., Kele, S., Fodor, L. & Swennen, R. (2017) Geobody architecture of continental spring carbonates: "Gazda" travertine quarry (Süttö, Gerecse Hills, Hungary). *Quaternary International*, *437*, 164–185.

UNESCO World Heritage Centre (1992–2015) Hierapolis – Pamukkale. Available at: http://whc.unesco.org/en/list/485/ [Accessed 24th August 2018].

Van Hinsbergen, D.J.J., Kaymakci, N., Spakman, W. & Torsvik, T.H. (2010) Reconciling the geological history of western Turkey with plate circuits and mantle tomography. *Earth and Planetary Science Letters*, *297*(3–4), 674–686.

Van Noten, K., Claes, H., Soete, J., Foubert, A., Özkul, M. & Swennen, R. (2013) Fracture networks and strike–slip deformation along reactivated normal faults in Quaternary travertine deposits, Denizli Basin, western Turkey. *Tectonophysics*, *588*, 154–170.

Van Noten, K., Topal, S., Baykara, M.O., Özkul, M., Claes, H., Aratman, C. et al. (2019) Pleistocene-Holocene tectonic reconstruction of the Ballık travertine (Denizli Graben, SW Turkey): (De)formation of large travertine geobodies at intersecting grabens. *Journal of Structural Geology*, *118*, 114–134.

Vincent, B., Fleury, M., Santerre, Y. & Brigaud, B. (2011) NMR relaxation of neritic carbonates: An integrated petrophysical and petrographical approach. *Journal of Applied Geophysics*, *74*(1), 38–58.

Wardlaw, N.C., McKellar, M. & Yu, L. (1988) Pore and throat size distributions determined by mercury porosimetry and by direct observation. *Carbonates and Evaporites*, *3*, 1–15.

Wardlaw, N.C. & Taylor, R.P. (1976) Mercury capillary pressure curves and the interpretation of pore structure and capillary behaviour in reservoir rocks. *Bulletin of Canadian Petroleum Geology*, *24*, 225–262.

Westphal, H., Surholt, I., Kiesl, C., Thern, H.F. & Kruspe, T. (2005) NMR measurements in carbonate rocks: Problems and an approach to a solution. *Pure and Applied Geophysics*, *162*(3), 549–570.

Wright, V.P. (2012) Lacustrine carbonates in rift settings: The interaction of volcanic and microbial processes on carbonate deposition. *Geological Society, London, Special Publications*, *370*(1), 39–47.

Wright, V.P. & Barnett, A.J. (2015) An abiotic model for the development of textures in some South Atlantic early Cretaceous lacustrine carbonates Cretaceous. *Geological Society, London, Special Publications*, *418*, 1–11.

Yao, Y. & Liu, D. (2012) Comparison of low-field NMR and mercury intrusion porosimetry in characterizing pore-size distributions of coals. *Fuel*, *95*, 152–158.

Zinszner, B. & Pellerin, F. (2007) *A geoscientist's guide to petrophysics*. Paris: IFP Publications, Editions Technips, pp. 1–384. Printed in France, Paris, 2007.

How to cite this article: Soete J, Claes S, Claes H, et al. Unravelling the pore network and its behaviour: An integrated NMR, MICP, XCT and petrographical study of continental spring carbonates from the Ballık area, SW Turkey. *Depositional Rec*. 2022;8:292–316. https://doi.org/10.1002/dep2.135